

# Multi-orbital Kondo screening in strongly correlated polyradical nanographenes.

Aitor Calvo-Fernández,<sup>1,2,\*</sup> Diego Soler-Polo,<sup>3,\*</sup> Andrés Pinar Solé,<sup>3,\*</sup> Shaotang Song,<sup>4,\*</sup> Oleksander Stetsovych,<sup>3</sup> Manish Kumar,<sup>3</sup> Guangwu Li,<sup>4</sup> Jishan Wu,<sup>4</sup> Jiong Lu,<sup>4,5</sup> Asier Eiguren,<sup>1,2,6</sup> María Blanco-Rey,<sup>7,2,8,†</sup> and Pavel Jelínek<sup>9,10,†</sup>

<sup>1</sup>*Departamento de Física, Universidad del País Vasco UPV-EHU, 48080 Leioa, Spain*

<sup>2</sup>*Donostia International Physics Center (DIPC), 20018 Donostia-San Sebastián, Spain*

<sup>3</sup>*Institute of Physics, Academy of Sciences of the Czech Republic,  
Cukrovarnicka 10, Prague 6, CZ 16200, Czech Republic*

<sup>4</sup>*Department of Chemistry, National University of Singapore, Singapore 117543, Singapore*

<sup>5</sup>*Institute for Functional Intelligent Materials,  
National University of Singapore, 117544, Singapore*

<sup>6</sup>*EHU Quantum Center, Universidad del País Vasco UPV-EHU, 48080 Leioa, Spain*

<sup>7</sup>*Departamento de Polímeros y Materiales Avanzados: Física, Química y Tecnología,  
Universidad del País Vasco UPV-EHU, 20018 Donostia-San Sebastián, Spain*

<sup>8</sup>*Centro de Física de Materiales CFM/MPC  
(CSIC-UPV/EHU), 20018 Donostia-San Sebastián, Spain*

<sup>9</sup>*Institute of Physics, Academy of Sciences of the Czech Republic, Prague, Czech Republic*

<sup>10</sup>*Regional Centre of Advanced Technologies and Materials,  
Czech Advanced Technology and Research Institute (CATRIN),  
Palacký University Olomouc, Olomouc 78371, Czech Republic*

(Dated: September 18, 2023)

## Abstract

We discuss coexistence of Kondo and spin excitation signals in tunneling spectroscopy in strongly correlated polyradical  $\pi$ -magnetic nanographenes on a metal surface. The Kondo signal is rationalized by a multi-orbital Kondo screening of the unpaired electrons. The fundamental processes are spin-flips of antiferromagnetic (AFM) order involving charged molecular multiplets. We introduce a perturbative model, which provides simple rules to identify the presence of AFM channels responsible for Kondo screening. The Kondo regime is confirmed by numerical renormalization group calculations. This framework can be applied to similar strongly correlated open-shell systems.

The molecular  $\pi$ -magnetism[1–3] has attracted the attention of researchers in various fields, including chemistry, physics, and materials science [4, 5]. Understanding the nature of  $\pi$ -magnetism and its underlying principles is crucial for the development of new materials and technologies, such as organic spintronics and molecular electronics [6]. Recent progress in on-surface synthesis [7, 8] combined with the unprecedented spatial resolution of scanning probe microscopy [9–11] has prompted new studies of  $\pi$ -magnetic systems [12–15].

From this point of view, one of the interesting magnetic phenomena is the observation of the Kondo effect [16, 17] in open-shell hydrocarbon molecules [18–22]. Originally, the Kondo effect was observed in adatoms with partially occupied  $d$ -electrons on metallic substrates [23–26]. In principle, the unpaired electrons in extended molecular orbitals can also act as a magnetic impurity and scatter the conduction electrons of the underlying metal surface, leading to the molecular Kondo effect [27–40].

While the conventional  $S = 1/2$  Kondo effect for magnetic impurities has been extensively studied and is very well understood, the mechanism of a multi-orbital Kondo effect of magnetic impurities with various strongly correlated unpaired electrons is barely explored. In particular, here the so-called underscreened Kondo effect can take place if there are less than  $2S$  screening channels [41], whereby the ground state shows a residual magnetic moment. This effect was extensively studied for quantum dot systems both experimentally [42, 43] and theoretically [44]. Recently, the Kondo effect was also reported for open-shell triplet ( $S = 1$ ) nanographenes [19, 22] and porphyrins [45–47] on metallic surfaces. The former case was theoretically rationalized within the one-crossing approximation [21]. Nev-

---

\* These authors contributed equally to this work.

† Corresponding author

ertheless, a broader picture of the multi-orbital Kondo effect in open-shell molecular systems is still missing. Models need to account, on the same footing, for aspects such as the number and symmetry of screening channels or the multiplet nature (i.e. many-electron) of the impurity electronic configuration. Therefore, the emergence of the Kondo resonances in open-shell nanographenes with several strongly correlated unpaired electrons on metallic surfaces provides a convenient platform for testing such general model.

In this work, we present a theoretical and experimental study of the multi-orbital Kondo effect in strongly correlated polyradical butterfly-shaped nanographenes deposited on a Au(111) surface. Interestingly, tunneling spectroscopy shows that the Kondo signal coexists with spin-excitation signals within the same nanographene (see Fig. 1). We build a three-step theoretical framework to explain this behaviour: (i) complete active space configuration interaction (CASCI) calculations [48] accurately provide the nanographene electronic states; (ii) a generalized perturbative analysis of the Anderson Hamiltonian, which accounts for the multiplet structure, reveals the antiferromagnetically coupled channels responsible for the Kondo screening by the metal substrate; and finally (iii) numerical renormalization group (NRG) calculations [49] provide observable quantities. We propose that the spatially-delocalized Kondo physics is ubiquitous in multireference systems (i.e. those that cannot be entirely described by a single Slater determinant) showing  $\pi$ -magnetism and can be tackled by our approach.

Recently, we reported on-surface synthesis of a tetraradical nanographene with a strongly correlated singlet ground state on Au(111) surface (for details see Ref. [50]). As side products of the reaction, we frequently found defective nanographenes, which arises from the detachment of methyl groups during cyclodehydrogenation reaction, leading to 1 or 2 pentagon rings on zig-zag edges (see Fig. 1). In the rest of the manuscript, we will refer as **1** (Fig. 1a) and **2** (Fig. 1b), respectively, to the nanographenes with one and two pentagon defects. Importantly, the presence of these defects significantly affects their electronic structure. Namely, we observe zero-energy resonances (see Fig. 1e,j), which are localized on the defect-free zig-zag edge (see Fig. 1c,h). To prove the magnetic origin of the zero-energy resonance we employed a nickelocene functionalized probe ( $S = 1$ ) [11]. Fig. S1 of the Supplemental Material (SM) [51] shows the strong renormalization of the spin-excitation signal in scanning tunneling spectroscopy (STS) spectra acquired along the tip approach, revealing the magnetic character of **1** and **2** [50]. Thus, we assign the zero-energy resonances to the

Kondo effect.

Interestingly, in the case of **1**, the STS spectra acquired at different positions of the molecule reveal a coexistence of an inelastic signal at 25 meV and a zero-bias Kondo resonance within the same molecule (see Fig. 1e). The inelastic signal, tentatively attributed to a spin excitation from the ground state to the first excited state, is located on a defect-free triangulene corner opposite to the zig-zag edge hosting the Kondo resonance (see Figs. S1 and S2).

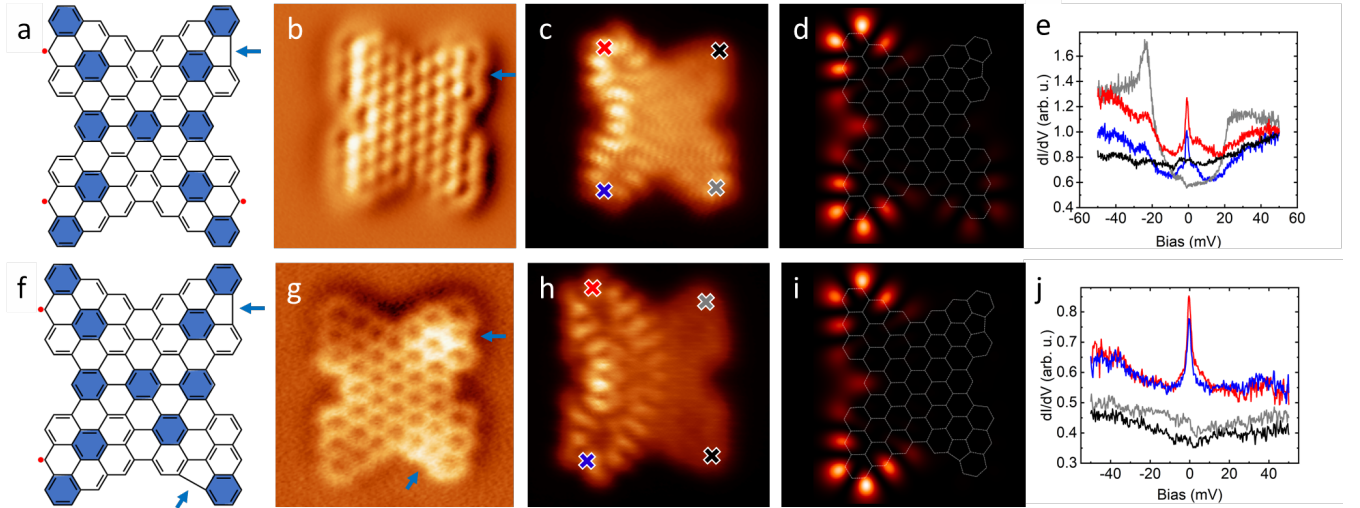


FIG. 1: Panels (a,f) display chemical structure of **1** and **2**, blue arrows highlight the location of the defects. Simultaneously recorded (b,g) high resolution CO tip atomic force microscopy and (c,h) corresponding STM images of the molecules acquired at 1 meV. (d,i) simulated  $dI/dV$  maps from the NTO for the spin-flip process between two degenerate ground states, (e,j)  $dI/dV$  spectra measured at the positions indicated by crosses on panels (c,h). The Kondo temperature  $T_K$  is estimated to be approx. 9.5K and 7.5K, respectively, using the Frota function [52]. Scanning range of the images: (b,c)  $3 \times 3 \text{ nm}^2$ , (g,h)  $2.5 \times 2.5 \text{ nm}^2$ .

To understand the electronic structure of **1** and **2** we employ the Hubbard model:

$$\hat{H} = t \sum_{\langle \mu, \nu \rangle, \sigma} \hat{c}_{\mu\sigma}^\dagger \hat{c}_{\nu\sigma} + \text{h.c.} + U \sum_{\mu} \hat{n}_{\mu\uparrow} \hat{n}_{\mu\downarrow}. \quad (1)$$

where  $\hat{c}_{\mu\sigma}^\dagger$  ( $\hat{c}_{\mu\sigma}$ ) are creation (annihilation) operators associated to the  $\mu$ -labelled Löwdin  $\pi$ -orbitals on a carbon atomic site with  $\sigma$  spin index,  $t$  represents hopping between the nearest

atomic sites, and  $U$  is the repulsive on-site Coulomb interaction introducing many-body electron-electron interaction in the system. We used values  $t = -2.8$  eV and  $U = 4.3$  eV, as parameterized for an effective Hubbard model in  $\pi$ -conjugated hydrocarbons [53].

Given the multireferential character of these systems, we solve the Hamiltonian eq. 1 by CASCI calculations in active spaces of up to six orbitals [48]. Fig. 2 displays the one-electron energy spectrum and corresponding Huckel orbitals selected for the spaces.

According to Hubbard CASCI(5,5) calculations **1** has a triradical duplet ( $S = 1/2$ ) ground state. Importantly, we observe that both the ground and excited states have strong multireferential character with contribution of several non-negligible Slater determinants (see Fig. 2c). We find that the first excited quartet state is 28 meV [51] higher than the ground state, which matches very well the experimentally observed spin excitation at 25 meV.

To rationalize the spatial distribution of the differential low-bias STM images shown in Fig. 1c,h, we calculate the natural transition orbitals [54] (NTO) corresponding to distinct spin-flip processes. In particular, we calculated the NTOs corresponding to the spin-flip process between two degenerate ground doublet states ( $|M_0, \pm 1/2\rangle$ ), see Fig. S6. The simulated STM image [55] from NTO shown in Fig. 1d fits nicely to the experiment (Fig. 1c). Similarly, we also calculated the NTO corresponding to the spin excitation from the doublet ground state  $|M_0, \pm 1/2\rangle$  and the first excited quartet state  $|M_1\rangle$ . Fig. S5 displays the calculated dI/dV maps of the corresponding NTO orbitals which match well to the experimental dI/dV map acquired at 24 meV (Fig. S2).

In the case of **2**, the ground state is a multi-reference diradical triplet ( $S = 1$ ) according to the Hubbard model solved using CASCI(6,6). It is almost exclusively formed by two determinants, with different occupation of singly-unoccupied/unoccupied molecular orbitals (see Fig. 2d). Fig. 1i displays calculated dI/dV map of NTOs corresponding to spin flip between two degenerated triplet states ( $|M_0, \pm 1\rangle$  and  $|M_0, 0\rangle$ ), which matches very well to the experimental dI/dV maps at zero bias, as shown in Fig. 1h.

One way to rationalize the presence of the Kondo effect could be the presence of an uncorrelated unpaired electron. In principle, this uncorrelated single electron could act as a  $S = 1/2$  magnetic impurity with Kondo screening mechanism by the bath of free electrons in the metallic surface. Thus, we evaluated the spin correlations,  $\langle \hat{S}_j \cdot \hat{S}_k \rangle - \langle \hat{S}_j \rangle \cdot \langle \hat{S}_k \rangle$ , between the three unpaired electrons in the doublet ground state (see SM [51]). The values in the

Tables S1 and S2 reveal strong entanglement between all unpaired electrons of **1** and **2**. Thus the presence of the Kondo effect cannot be explained within the traditional framework of a  $S = 1/2$  magnetic impurity screened by a bath of free electrons of the metal.

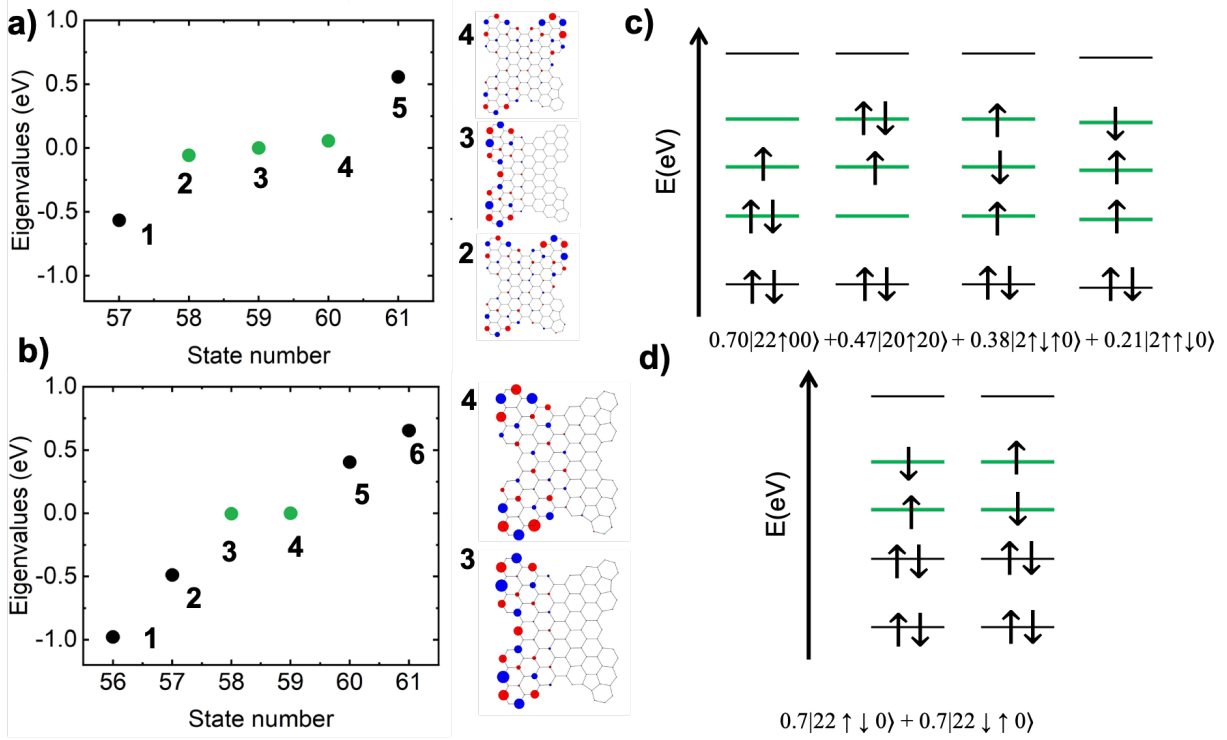


FIG. 2: Panels (a,b) show the single electron Hückel energy spectrum and the corresponding frontier orbitals of **1** and **2**, respectively. In green we highlight the orbitals that are considered later in the NRG calculations. Panels (c,d) display a scheme of the multi-referential ground state obtained from Hubbard-CASCI(5,5) (resp. CASCI(6,6)) for **1** and **2**. For more details about the electronic structure, see discussion in SM [51].

The emergence of Kondo peaks is explained here with the ionic multichannel Anderson Hamiltonian [56], which is converted into a Kondo Hamiltonian by application of a Schrieffer-Wolf canonical transformation [57, 58]. This filters out high-energy fluctuations, keeping second order scattering processes. The starting molecule-substrate hybridization contribution has the form

$$\hat{H}_{\text{hyb}} = \int_{-D}^D d\epsilon \rho^{\frac{1}{2}} V \langle M_f m_f | \hat{f}_{\alpha\sigma}^\dagger | M_i m_i \rangle | M_f m_f \rangle \langle M_i m_i | \hat{c}_{\epsilon\alpha\sigma} + \text{h.c.}, \quad (2)$$

where  $V$  is the hybridization amplitude, repeated indices are summed over and the integral is made over a conduction band of width  $2D$  and constant density of states  $\rho$ . Since

the molecular orbitals (MO) are orthogonal and their substrate-mediated hybridization is small, we assume that each channel couples to one specific CASCI active space MO, both labeled  $\alpha$ . [59]. Each term introduces electron-hole pair excitations amounting to creation (annihilation) of an electron in the MO  $\alpha$  by the operator  $\hat{f}_{\alpha\sigma}^\dagger$  ( $\hat{f}_{\alpha\sigma}$ ) and annihilation (creation) of a conduction electron by the operator  $\hat{c}_{\epsilon\alpha\sigma}$  ( $\hat{c}_{\epsilon\alpha\sigma}^\dagger$ ). The multiplet states are labeled  $|Mm\rangle$ . Aside from the ground multiplet  $M_0$ , we keep only the charged multiplets  $M_c$  with the lowest energy, which are obtained also from CASCI calculations by removing or adding one electron within the same active space. These are the main contributions to the molecule Kondo physics (explicit expressions are given in SM section S3[51]).

The Kondo Hamiltonian resulting from the canonical transformation is

$$\hat{H}_K = \frac{J_{\alpha\alpha'}}{2} \hat{\mathbf{S}} \cdot \hat{\mathbf{s}}_{\alpha\alpha'} \quad (3)$$

where  $J_{\alpha\alpha'}$  are the effective coupling constants,  $\hat{\mathbf{S}}$  is the molecular spin operator, and  $\hat{\mathbf{s}}_{\alpha\alpha'}$  are the conduction spin density matrix elements at the locations of the MOs  $\alpha$  and  $\alpha'$  [60]. The obtained expressions for  $J_{\alpha\alpha'}$  are (see SM section S4[51])

$$J_{\alpha\alpha'} = \sum_{M_c} \frac{V^2}{\epsilon_{M_c} - \epsilon_{M_0}} C_{\alpha\alpha'}^{M_c}, \quad (4)$$

$$C_{\alpha\alpha'}^{M_c} = \begin{cases} \frac{\langle M_0 | \hat{f}_\alpha | M_c \rangle \langle M_c | \hat{f}_{\alpha'}^\dagger | M_0 \rangle}{(S_0 + \frac{1}{2})}, & N_0 + 1, S_0 - \frac{1}{2}, \\ \frac{\langle M_0 | \hat{f}_{\alpha'}^\dagger | M_c \rangle^* \langle M_c | \hat{f}_\alpha | M_0 \rangle^*}{S_0}, & N_0 - 1, S_0 - \frac{1}{2}, \\ -\frac{\langle M_0 | \hat{f}_\alpha | M_c \rangle \langle M_c | \hat{f}_{\alpha'}^\dagger | M_0 \rangle}{(S_0 + \frac{1}{2})}, & N_0 + 1, S_0 + \frac{1}{2}, \\ -\frac{\langle M_0 | \hat{f}_{\alpha'}^\dagger | M_c \rangle^* \langle M_c | \hat{f}_\alpha | M_0 \rangle^*}{(S_0 + 1)}, & N_0 - 1, S_0 + \frac{1}{2}. \end{cases} \quad (5)$$

where each coefficient  $C_{\alpha\alpha'}^{M_c}$  is determined by the number of particles ( $N_0 \pm 1$ ) and the spin ( $S_0 \pm \frac{1}{2}$ ) of the excited multiplet  $M_c$ .

The coupling constants  $J_{\alpha\alpha'}$  form a hermitian matrix  $\mathbf{J}$  that can be diagonalized to rewrite the effective interaction as  $H_K = j_a \hat{\mathbf{S}} \cdot \hat{\mathbf{s}}_{aa}$ , where  $j_a$  are the eigenvalues and  $|a\rangle = U_{\alpha a} |\alpha\rangle$  the corresponding rotated MOs, which we denote *Kondo orbitals*.  $j_a > 0$  means that the coupling is antiferromagnetic (AFM) and  $j_a < 0$  ferromagnetic (FM). The latter does not qualitatively alter the low-temperature physics of the system. Therefore, the regions where Kondo effects are observed are those where Kondo orbitals  $|a\rangle$  such that  $j_a > 0$  are localized, offering a rigorous alternative to NTOs in the interpretation of dI/dV maps (see SM section S4 D and

$M_c$	$M_{0-}$	$M_{1-}$	$M_{0+}$	$M_{1+}$	
$\alpha$	2	0.86	0	-0.53	0
	3	0	0.75	-0.07	-0.71
	4	-0.26	0	-0.63	0
$M_c$	$M_{0-}$	$M_{1-}$	$M_{0+}$	$M_{1+}$	
$\alpha$	3	0.77	0.80	0.95	0.98
	4	-0.52	0.53	0.63	0.65

TABLE I: Reduced matrix elements  $\langle M_c | \hat{f}_\alpha^{(\dagger)} | M_0 \rangle$  for positively (+) and negatively (-) charged excited multiplets  $M_c$  for **1** (top table) and **2** (bottom table).

Figs. S7 and S8). Thus expressions in eq.5 represent a simple rule to identify AFM channels responsible for Kondo screening.

For **1** we use a 3-channel Anderson model, with each channel coupled to one of the 3 MOs highlighted in green in Fig. 2, labeled  $\alpha = 2, 3, 4$ , since these are the only ones with a sizeable magnetic coupling to the molecule. The necessary data for computing the coupling constants for these channels are given in Table I. The energies  $\epsilon_M$  have been approximated as  $\epsilon_- = \epsilon_{M_{0-}} = \epsilon_{M_{1-}}$  and  $\epsilon_+ = \epsilon_{M_{0+}} = \epsilon_{M_{1+}}$ . Using eq. 4, the matrix  $\mathbf{J}$  is, up to two digits of precision in the coefficients,

$$\mathbf{J} = V^2 \begin{pmatrix} -\frac{0.40}{\epsilon_-} - \frac{0.29}{\epsilon_+} & -\frac{0.06}{\epsilon_+} & 0 \\ -\frac{0.06}{\epsilon_-} & \frac{1.13}{\epsilon_-} + \frac{0.51}{\epsilon_+} & 0 \\ 0 & 0 & -\frac{0.04}{\epsilon_-} - \frac{0.4}{\epsilon_+} \end{pmatrix} \quad (6)$$

The only positive eigenvalue  $j_a$  couples the molecular spin primarily to channel  $\alpha = 3$ , with a small mixing  $|U_{23}|^2 \sim 0.001$  with  $\alpha = 2$ . Therefore, we predict a Kondo resonance to be located primarily in the orbital 3 region. This is in agreement with the experimental results, which show a strong Kondo signal in the left wing of the molecule, where the Hückel orbital 3 is located (see Figs. 1 and 2).

For **2**, the channels contributing to the magnetic coupling are those highlighted in green in Fig. 2, labeled  $\alpha = 3, 4$ . Following the same procedure as for **1**, we use the data in Table I to obtain

$$\mathbf{J} = V^2 \begin{pmatrix} \frac{1.24}{\epsilon_-} + \frac{1.24}{\epsilon_+} & \frac{0.1}{\epsilon_-} + \frac{0.83}{\epsilon_+} \\ \frac{0.1}{\epsilon_-} + \frac{0.83}{\epsilon_+} & \frac{0.57}{\epsilon_-} + \frac{0.55}{\epsilon_+} \end{pmatrix}. \quad (7)$$

For values of  $\epsilon_-$  and  $\epsilon_+$  compatible with the formation of a local moment, both eigenvalues  $j_a$  are positive and of the same order of magnitude (see SM [51]). This places the Kondo signal primarily in the left wing of **2**, as seen in the experiments, see Fig.1.

To corroborate the results obtained above, we compute the orbital-resolved spectral functions by means of NRG [49, 61] on a two-channel Anderson model. For **1**, we remove the  $\alpha = 4$  channel, as it has negligible magnetic coupling to the molecule. The hybridization parameter  $\Gamma = \pi\rho V^2$  for each system is chosen so that the full width at half peak is of the order of the Kondo temperature  $k_B T_K \simeq 10$  K found in experiment (see Fig. 1). Details of the procedure can be found in the SM section S5[51].

For **1**, the calculated spectral functions for  $\epsilon_- = 0.12$ ,  $\epsilon_+ = 0.29$ , and a hybridization  $\Gamma = 0.1$ , all in units of the half-bandwidth  $D = 1$  eV, are shown in Fig. 3. The appearance of a clear Kondo peak only in the channel coupled to the MO 3 supports our prediction that the effective AFM coupling to the molecule happens primarily through channel 3. Thus, the conclusions from the previous section hold even for the large hybridization values. For **2**, the calculated spectral functions for  $\epsilon_- = 0.155$ ,  $\epsilon_+ = 0.3$ , and  $\Gamma = 0.15$  are shown in Fig. 3. Very similar Kondo peaks are found in the vicinity of both orbitals, as expected from our previous discussion.

In conclusion, we presented strongly correlated polyradical nanographenes showing coexistence of spatially delocalized Kondo and spin-flip excitation. We developed a perturbative approach of spin-flip excitation between various molecular multiplets, which enables us to identify the presence of antiferromagnetic screening channels. NRG calculations confirmed that AFM screening channels are responsible for multi-orbital Kondo screening in the polyradical nanographenes. We introduced the concept of the Kondo orbitals obtained from diagonalization of the magnetic exchange coupling matrix, which allow us to map a real-space localization of the Kondo resonance. We anticipate that the presented theoretical framework can be adopted for analysis of the emergence of the Kondo regime in other strongly correlated polyradical atomic and molecular systems.

## ACKNOWLEDGMENTS

A.C.-F., A.E. and M.B.-R. acknowledge grants No. IT-1527-22, funded by the Department of Education, Universities and Research of the Basque Government, and No. PID2019-

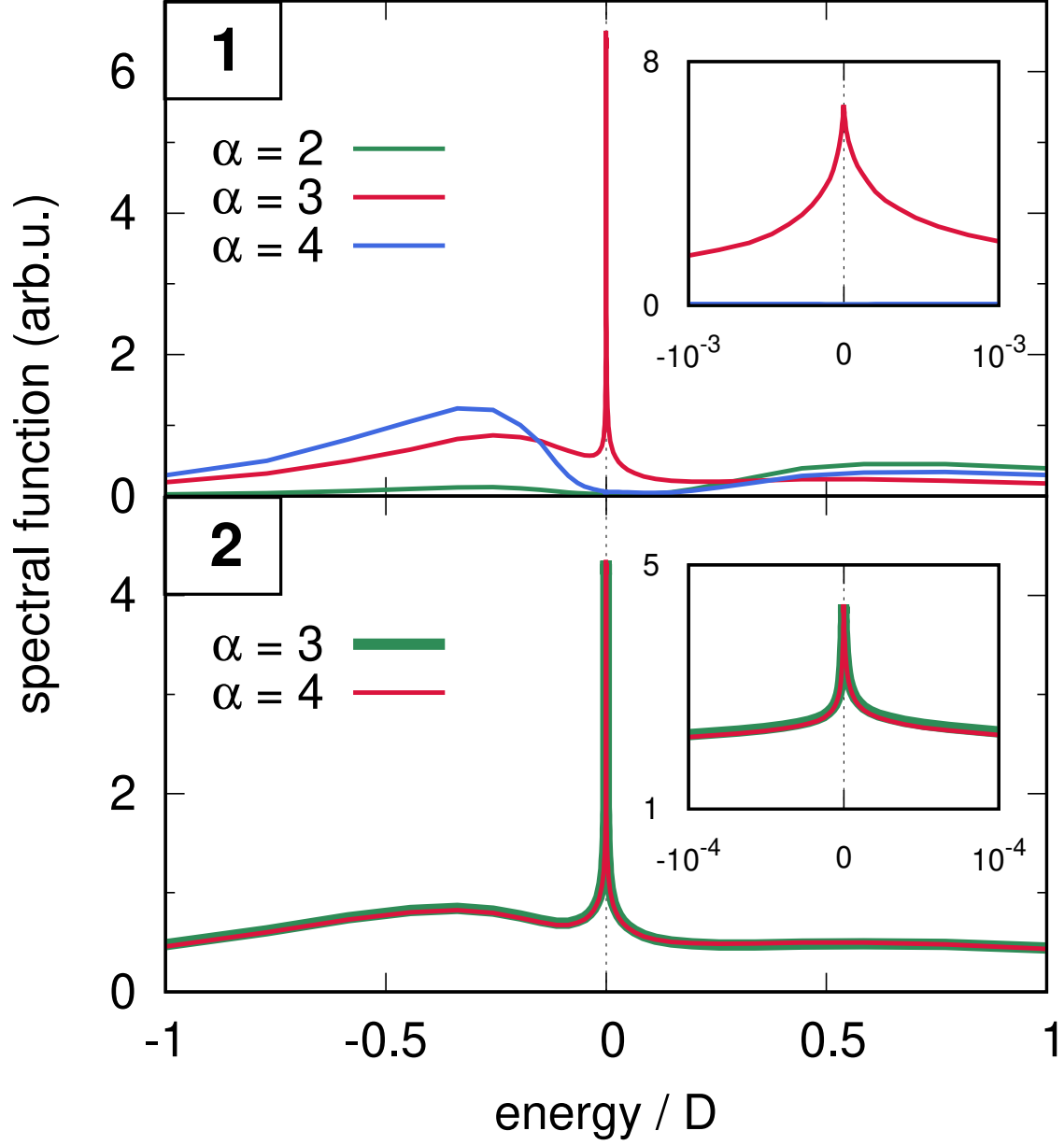


FIG. 3: Orbital-resolved spectral functions for **1** (top panel) and **2** (bottom panel). Insets: low-energy close-up.

103910GB-I00, funded by MCIN/AEI 10.13039/501100011033/. A.C.-F. acknowledges grant No. PRE2020-092046 funded by the Spanish MCIN. D.S., A.P., O.S., M.K. and P.J. acknowledge financial support from the CzechNanoLab Research Infrastructure supported by MEYS CR (LM2023051) and the GACR project no. 23-05486S. J. Lu acknowledges the support from MOE grants (MOE T2EP50121-0008 and MOE-T2EP10221-0005) We acknowledge

fruitful discussion with L. Veis and A. Matej.

---

- [1] A. A. Ovchinnikov, *Theoretica chimica acta* **47**, 297 (1978).
- [2] E. H. Lieb, *Phys. Rev. Lett.* **62**, 1201 (1989).
- [3] R. Ortiz, R. A. Boto, N. García-Martínez, J. C. Sancho-García, M. Melle-Franco, and J. Fernández-Rossier, *Nano Letters* **19**, 5991 (2019).
- [4] D. G. de Oteyza and T. Frederiksen, *Journal of Physics: Condensed Matter* **34**, 443001 (2022).
- [5] O. V. Yazyev, *Reports on Progress in Physics* **73**, 056501 (2010).
- [6] J. Veciana, D. Arçon, M. Deumal, K. Inoue, M. Kinoshita, J. J. Novoa, F. Palacio, K. Prasad, J. M. Rawson, and C. Rovira, eds.,  *$\pi$ -Electron Magnetism* (Springer Berlin Heidelberg, 2001).
- [7] L. Grill, M. Dyer, L. Lafferentz, M. Persson, M. V. Peters, and S. Hecht, *Nature Nanotechnology* **2**, 687 (2007).
- [8] S. Clair and D. G. de Oteyza, *Chemical Reviews* **119**, 4717 (2019).
- [9] L. Gross, F. Mohn, N. Moll, P. Liljeroth, and G. Meyer, *Science* **325**, 1110 (2009).
- [10] P. Jelínek, *Journal of Physics: Condensed Matter* **29**, 343002 (2017).
- [11] M. Ormaza, N. Bachellier, M. N. Faraggi, B. Verlhac, P. Abufager, P. Ohresser, L. Joly, M. Romeo, F. Scheurer, M.-L. Bocquet, N. Lorente, and L. Limot, *Nano Letters* **17**, 1877 (2017).
- [12] N. Pavliček, A. Mistry, Z. Majzik, N. Moll, G. Meyer, D. J. Fox, and L. Gross, *Nature Nanotechnology* **12**, 308 (2017).
- [13] S. Mishra, D. Beyer, K. Eimre, S. Kezilebieke, R. Berger, O. Gröning, C. A. Pignedoli, K. Müllen, P. Liljeroth, P. Ruffieux, X. Feng, and R. Fasel, *Nature Nanotechnology* **15**, 22 (2019).
- [14] P. Ruffieux, S. Wang, B. Yang, C. Sánchez-Sánchez, J. Liu, T. Dienel, L. Talirz, P. Shinde, C. A. Pignedoli, D. Passerone, T. Dumslaff, X. Feng, K. Müllen, and R. Fasel, *Nature* **531**, 489 (2016).
- [15] S. Song, J. Su, M. Telychko, J. Li, G. Li, Y. Li, C. Su, J. Wu, and J. Lu, *Chem. Soc. Rev.* **50**, 3238 (2021).
- [16] A. C. Hewson, *The Kondo Problem to Heavy Fermions*, Cambridge Studies in Magnetism

- (Cambridge University Press, 1993).
- [17] J. Kondo, Progress of theoretical physics **32**, 37 (1964).
  - [18] J. Li, S. Sanz, M. Corso, D. J. Choi, D. Peña, T. Frederiksen, and J. I. Pascual, Nature Communications **10**, 10.1038/s41467-018-08060-6 (2019).
  - [19] J. Li, S. Sanz, J. Castro-Esteban, M. Vilas-Varela, N. Friedrich, T. Frederiksen, D. Peña, and J. I. Pascual, Phys. Rev. Lett. **124**, 177201 (2020).
  - [20] S. Mishra, D. Beyer, K. Eimre, S. Kezilebieke, R. Berger, O. Gröning, C. A. Pignedoli, K. Müllen, P. Liljeroth, P. Ruffieux, X. Feng, and R. Fasel, Nature Nanotechnology **15**, 22 (2020).
  - [21] D. Jacob, R. Ortiz, and J. Fernández-Rossier, Phys. Rev. B **104**, 075404 (2021).
  - [22] E. Turco, A. Bernhardt, N. Krane, L. Valenta, R. Fasel, M. Juríček, and P. Ruffieux, JACS Au **3**, 1358 (2023).
  - [23] V. Madhavan, W. Chen, T. Jamneala, M. F. Crommie, and N. S. Wingreen, Science **280**, 567 (1998).
  - [24] J. Li, W.-D. Schneider, R. Berndt, and B. Delley, Phys. Rev. Lett. **80**, 2893 (1998).
  - [25] N. Knorr, M. A. Schneider, L. Diekhöner, P. Wahl, and K. Kern, Phys. Rev. Lett. **88**, 096804 (2002).
  - [26] A. F. Otte, M. Ternes, K. von Bergmann, S. Loth, H. Brune, C. P. Lutz, C. F. Hirjibehedin, and A. J. Heinrich, Nature Physics **4**, 847 (2008).
  - [27] T. Esat, T. Deilmann, B. Lechtenberg, C. Wagner, P. Krüger, R. Temirov, F. B. Anders, M. Rohlfing, and F. S. Tautz, Physical Review B **91**, 10.1103/physrevb.91.144415 (2015).
  - [28] G. D. Scott and D. Natelson, ACS Nano **4**, 3560 (2010).
  - [29] T. Komeda, H. Isshiki, J. Liu, Y.-F. Zhang, N. Lorente, K. Katoh, B. K. Breedlove, and M. Yamashita, Nature Communications **2**, 217 (2011).
  - [30] E. Minamitani, N. Tsukahara, D. Matsunaka, Y. Kim, N. Takagi, and M. Kawai, Phys. Rev. Lett. **109**, 086602 (2012).
  - [31] R. Hiraoka, E. Minamitani, R. Arafune, N. Tsukahara, S. Watanabe, M. Kawai, and N. Takagi, Nature Communications **8**, 16012 (2017).
  - [32] R. Žitko, G. G. Blesio, L. O. Manuel, and A. A. Aligia, Nature Communications **12**, 6027 (2021).
  - [33] I. Fernández-Torrente, K. J. Franke, and J. I. Pascual, Phys. Rev. Lett. **101**, 217203 (2008).

- [34] T. Choi, S. Bedwani, A. Rochefort, C.-Y. Chen, A. J. Epstein, and J. A. Gupta, *Nano Letters* **10**, 4175 (2010).
- [35] U. G. E. Perera, H. J. Kulik, V. Iancu, L. G. G. V. Dias da Silva, S. E. Ulloa, N. Marzari, and S.-W. Hla, *Phys. Rev. Lett.* **105**, 106601 (2010).
- [36] R. Requist, S. Modesti, P. P. Baruselli, A. Smogunov, M. Fabrizio, and E. Tosatti, *Proceedings of the National Academy of Sciences* **111**, 69 (2014).
- [37] E. Minamitani, Y.-S. Fu, Q.-K. Xue, Y. Kim, and S. Watanabe, *Phys. Rev. B* **92**, 075144 (2015).
- [38] L. L. Patera, S. Sokolov, J. Z. Low, L. M. Campos, L. Venkataraman, and J. Repp, *Angewandte Chemie International Edition* **58**, 11063 (2019).
- [39] H. Koshida, H. Okuyama, S. Hatta, T. Aruga, and E. Minamitani, *Phys. Rev. B* **103**, 155412 (2021).
- [40] S. Lu, H. Nam, P. Xiao, M. Liu, Y. Guo, Y. Bai, Z. Cheng, J. Deng, Y. Li, H. Zhou, G. Henkelman, G. A. Fiete, H.-J. Gao, A. H. MacDonald, C. Zhang, and C.-K. Shih, *Phys. Rev. Lett.* **127**, 186805 (2021).
- [41] Nozières, Ph. and Blandin, A., *J. Phys. France* **41**, 193 (1980).
- [42] N. Roch, S. Florens, T. A. Costi, W. Wernsdorfer, and F. Balestro, *Phys. Rev. Lett.* **103**, 197202 (2009).
- [43] J. J. Parks, A. R. Champagne, T. A. Costi, W. W. Shum, A. N. Pasupathy, E. Neuscamman, S. Flores-Torres, P. S. Cornaglia, A. A. Aligia, C. A. Balseiro, G. K.-L. Chan, H. D. A. na, and D. C. Ralph, *Science* **328**, 1370 (2010).
- [44] M. Pustilnik and L. I. Glazman, *Phys. Rev. Lett.* **87**, 216601 (2001).
- [45] J. Girovsky, J. Nowakowski, M. E. Ali, M. Baljovic, H. R. Rossmann, T. Nijs, E. A. Aeby, S. Nowakowska, D. Siewert, G. Srivastava, C. Wäckerlin, J. Dreiser, S. Decurtins, S.-X. Liu, P. M. Oppeneer, T. A. Jung, and N. Ballav, *Nature Communications* **8**, 15388 (2017).
- [46] K. Biswas, M. Urbani, A. Sánchez-Grande, D. Soler-Polo, K. Lauwaet, A. Matěj, P. Mutombo, L. Veis, J. Brabec, K. Pernal, J. M. Gallego, R. Miranda, D. Écija, P. Jelínek, T. Torres, and J. I. Urgel, *Journal of the American Chemical Society* **144**, 12725 (2022).
- [47] Q. Sun, L. M. Mateo, R. Robles, P. Ruffieux, N. Lorente, G. Bottari, T. Torres, and R. Fasel, *Journal of the American Chemical Society* **142**, 18109 (2020).
- [48] B. O. Roos, P. R. Taylor, and P. E. Sigbahn, *Chemical Physics* **48**, 157 (1980).

- [49] H. R. Krishna-Murthy, J. W. Wilkins, and K. G. Wilson, *Physical Review B* **21**, 1003 (1980).
- [50] S. Song, A. P. Solé, A. Matěj, G. Li, O. Stetsovych, D. Soler, H. Yang, M. Telychko, J. Li, M. Kumar, J. Brabec, L. Veis, J. Wu, P. Jelinek, and J. Lu, Highly-entangled polyradical nanographene with coexisting strong correlation and topological frustration (2023), arXiv:2304.01641 [cond-mat.mtrl-sci].
- [51] See Supplemental Material, which includes additional Refs. [62–67], for further details.
- [52] H. Prüser, M. Wenderoth, A. Weismann, and R. G. Ulbrich, *Physical Review Letters* **108**, 10.1103/physrevlett.108.166604 (2012).
- [53] M. Schüler, M. Rösner, T. O. Wehling, A. I. Lichtenstein, and M. I. Katsnelson, *Phys. Rev. Lett.* **111**, 036601 (2013).
- [54] R. L. Martin, *The Journal of Chemical Physics* **118**, 4775 (2003).
- [55] O. Krejčí, P. Hapala, M. Ondráček, and P. Jelínek, *Physical Review B* **95**, 10.1103/physrevb.95.045407 (2017).
- [56] P. W. Anderson, *J. Phys. C: Solid St. Phys* **3** (1970).
- [57] J. R. Schrieffer and P. A. Wolff, *J. Kondo, Progr. Theoret. Phys. (Kyoto)* **14**, 61 (1966).
- [58] F. Flores and E. C. Goldberg, *Journal of Physics: Condensed Matter* **29**, 055602 (2016).
- [59] Since the MOs are orthogonal and their substrate-mediated hybridization is small, we consider the approximation that each channel couples to one specific MO only.
- [60] We have neglected the potential scattering term, as it does not affect the spin of the molecule.
- [61] R. Bulla, T. A. Costi, and T. Pruschke, *Rev. Mod. Phys.* **80**, 395 (2008).
- [62] A. Cahlik, Kondo fit, [https://github.com/cahlikales/Kondo\\_fit](https://github.com/cahlikales/Kondo_fit).
- [63] H. Frota, *Physical Review B* **45**, 1096 (1992).
- [64] M. Gruber, A. Weismann, and R. Berndt, *Journal of Physics: Condensed Matter* **30**, 424001 (2018).
- [65] M. Yoshida, M. A. Whitaker, and L. N. Oliveira, *Phys. Rev. B* **41**, 9403 (1990).
- [66] A. Calvo-Fernández, M. Blanco-Rey, and A. Eiguren, The PointGroupNRG code for numerical renormalization group calculations with discrete point-group symmetries (2023), arXiv:2307.03658 [cond-mat.str-el].
- [67] C. Jayaprakash, H. R. Krishna-murthy, and J. W. Wilkins, *Phys. Rev. Lett.* **47**, 737 (1981).

# Supplemental Material for “Multi-orbital Kondo screening in strongly correlated polyradical nanographenes”

Aitor Calvo-Fernández,<sup>1,2</sup> Diego Soler-Polo,<sup>3</sup> Andrés Pinar Solé,<sup>3</sup> Shaotang Song,<sup>4</sup> Oleksander Stetsovych,<sup>3</sup> Manish Kumar,<sup>3</sup> Guangwu Li,<sup>4</sup> Jishan Wu,<sup>4</sup> Jiong Lu,<sup>4,5</sup> Asier Eiguren,<sup>1,2,6</sup> María Blanco-Rey,<sup>7,2,8</sup> and Pavel Jelínek<sup>9,10</sup>

<sup>1</sup>*Departamento de Física, Universidad del País Vasco UPV-EHU, 48080 Leioa, Spain*

<sup>2</sup>*Donostia International Physics Center (DIPC), 20018 Donostia-San Sebastián, Spain*

<sup>3</sup>*Institute of Physics, Academy of Sciences of the Czech Republic,  
Cukrovarnicka 10, Prague 6, CZ 16200, Czech Republic*

<sup>4</sup>*Department of Chemistry, National University of Singapore, Singapore 117543, Singapore*

<sup>5</sup>*Institute for Functional Intelligent Materials,  
National University of Singapore, 117544, Singapore*

<sup>6</sup>*EHU Quantum Center, Universidad del País Vasco UPV-EHU, 48080 Leioa, Spain*

<sup>7</sup>*Departamento de Polímeros y Materiales Avanzados: Física, Química y Tecnología,  
Universidad del País Vasco UPV-EHU, 20018 Donostia-San Sebastián, Spain*

<sup>8</sup>*Centro de Física de Materiales CFM/MPC  
(CSIC-UPV/EHU), 20018 Donostia-San Sebastián, Spain*

<sup>9</sup>*Institute of Physics, Academy of Sciences of the Czech Republic, Prague, Czech Republic*

<sup>10</sup>*Regional Centre of Advanced Technologies and Materials,  
Czech Advanced Technology and Research Institute (CATRIN),  
Palacký University Olomouc, Olomouc 78371, Czech Republic*

(Dated: September 18, 2023)

## S1. EXPERIMENTS

The low-temperature SPM experiments were performed using a commercial low-temperature (1.2 K) STM/nc-AFM microscope Specs-JT with a Kolibri sensor ( $f \approx 1$  MHz) with a Stanford Lock-in amplifier. High-resolution AFM and  $dI/dV$  maps were performed using a functionalized tip with a single carbon monoxide (CO) molecule. CO was dosed to the Au(111) at 4K. Typical CO coverages of two-three molecules per  $20 \times 20$  nm<sup>2</sup> sample scan area were used. CO was picked up from the Au(111) by placing the tip on top of the molecule and increasing the sample bias in constant height STM mode until the CO functionalizes the tip ( $\approx 200$  pA at 130mV). The high-resolution AFM imaging was performed at constant height mode with bias voltage of 1 mV with oscillation amplitude of 50 pm. Lock-in parameters during  $dI/dV$  measurements: frequency: 723 Hz, modulation amplitude: 0.5 mV, time constant: 30 ms.

Nickelocene (NiCp<sub>2</sub>) was dosed from a tantalum pocket kept at room temperature onto the prepared samples on Au(111) with submonolayer coverage at  $T < 4$ K. To pick up the NiCp<sub>2</sub> on the STM tip, the sample was scanned at low current (10 pA STM setpoint and below 5 mV sample bias) until the nickelocene functionalizes the tip. Only stable NiCp<sub>2</sub> tips were used for IETS measurements. Additionally, the NiCp<sub>2</sub> tips were tested prior measurements by performing  $d^2I/dV^2(z)$  on Au(111) to observe the characteristic IETS peaks at  $\approx 4$  mV of the unperturbed NiCp<sub>2</sub> molecule.

The fitting of the Kondo peaks was done with a Python script [1] that includes fitting routines with a Frota function [2] and a thermally broadened Fano function [3], where an operator is defined for the convolution of the Fano line-shape with a derivative of Fermi-Dirac distribution. The fitting was performed with Model class in LMFIT, using Levenberg-Marquardt least-squares method.

### A. Magnetic origin of zero-bias peaks

To demonstrate the magnetic origin of zero energy peaks observed in STS spectra, shown in Figure 1 in the main text, we carried out STS measurements with nickelocene-functionalized tip. Figure S1 displays the STS spectra measured along tip approach towards the sample, which clearly show a strong renormalization of the spin-excitation of the nick-

elocene tip at 5 meV along the tip approach due to exchange interaction between the spin of nickelocene tip and products **1** and **2**, respectively.

## S2. CALCULATIONS

### A. Natural transition orbitals

To calculate Natural Transition Orbitals (NTO) orbitals between two states,  $|\Psi_-\rangle$  and  $|\Psi_+\rangle$  we construct for each  $j$  and  $k$  the matrix element:

$$T_{j,k} = \langle \Psi_- | \hat{f}_{j\downarrow}^\dagger \hat{f}_{k\uparrow} | \Psi_+ \rangle,$$

where, as above,  $j$  is an index labeling molecular orbitals and  $\hat{f}_{j\sigma}^\dagger$  are the creation operators for electrons in molecular spin-orbital  $j\sigma$ . We then proceed, following Martin [5], to diagonalize the matrix  $TT^\dagger$  to obtain the NTOs. Finally, we use the PP-STM code [6] to calculate corresponding  $dI/dV$  maps using s-like tip.

### B. Spin-spin correlation of unpaired electrons

We evaluated the spin correlations between the unpaired electrons in the degenerate ground states of products **1** and **2** as follows:

$$\langle \Psi_0 | \vec{S}_j \cdot \vec{S}_k | \Psi_0 \rangle - \langle \Psi_0 | \vec{S}_j | \Psi_0 \rangle \cdot \langle \Psi_0 | \vec{S}_k | \Psi_0 \rangle,$$

where the indices  $j$  and  $k$  design the molecular orbitals. Here negative correlation represents antiferromagnetic coupling and positive ferromagnetic coupling between unpaired spins. We should note that the strong entanglement between three unpaired electrons is independent of the choice of the MO basis set.

The correlations between the unpaired spins are summarized in the Tables S1 and S2, where the molecular orbital "3" is the single-occupied zero-mode that survives on the butterfly after introducing the defect.

### C. Electronic structure of product 1: CASCI calculations

Here we describe the wave-function of the ground and excited states of **1** obtained from CASCI calculations for neutral ( $N$ ) and charged ( $N \pm 1$ ) states.

	2	3	4
2	0.050	-0.060	0.014
3	-0.060	0.127	-0.062
4	0.014	-0.062	0.052

TABLE S1: Spin-spin correlations in **1** for the doublet ground state in basis of Hückel molecular orbitals of the active space shown in Fig.S3.

	3	4
3	0.25	-0.24
4	-0.24	0.25

TABLE S2: Spin-spin correlations in the **2** for the doublet ground state in basis of Hückel molecular orbitals of the active space shown in Fig.S4.

**Neutral molecule:**

The **1** wave-function in its doublet ground state in the  $S_z = 1/2$  subspace is given by:

$$|M_0\rangle \approx 0.70|2 \uparrow 0\rangle + 0.47|0 \uparrow 2\rangle + 0.38|\uparrow\downarrow\uparrow\rangle + 0.21|\uparrow\uparrow\downarrow\rangle,$$

whereas the  $S_z = -1/2$  is obtained by applying the spin lowering operator.

The quadruplet excited state **1**, located at 25 meV of the doublet ground state, has a somewhat simpler structure in the subspace  $S_z = 1/2$ :

$$|M_1, S_z = 1/2\rangle \approx 0.57|\uparrow\uparrow\downarrow\rangle + 0.57|\uparrow\downarrow\uparrow\rangle + 0.57|\downarrow\uparrow\uparrow\rangle.$$

In the two equations above, orbitals 1 and 5 are dismissed, since their occupations are 2 and 0, and do not change.

**Molecule with one extra electron:** The two main multiplets in the subspace  $S_z = 0$  are

$$|M_0^+, S_z = 0\rangle \approx 0.64|22 \uparrow\downarrow 0\rangle + 0.64|22 \downarrow\uparrow 0\rangle + 0.13|2 \uparrow 2 \downarrow 0\rangle + 0.13|2 \downarrow 2 \uparrow 0\rangle - 0.14|2 \uparrow\downarrow\uparrow\downarrow\rangle + 0.14|2 \downarrow\uparrow\downarrow\uparrow\rangle,$$

$$|M_1^+, S_z = 0\rangle \approx -0.72|22200\rangle + 0.38|22020\rangle,$$

whereas in the  $S_z = 1$  subspace we have

$$|M_0^+, S_z = 1\rangle \approx -0.91|22 \uparrow \uparrow 0\rangle - 0.18|2 \uparrow 2 \uparrow 0\rangle - 0.19|2 \uparrow \uparrow \downarrow\rangle - 0.11|22 \uparrow 0 \uparrow\rangle - 0.11|2 \uparrow \uparrow 20\rangle.$$

Their energies with respect to the ground state of the neutral molecule (CAS(5,5) for the Hubbard hamiltonian) are respectively: 487 meV and 491 meV.

**Molecule with one less electron ( $N - 1$ ):** The two main multiplets are

$$|M_0^-, S_z = 0\rangle \approx 0.70|2 \uparrow \downarrow 00\rangle + 0.70|2 \downarrow \uparrow 00\rangle,$$

$$|M_0^-, S_z = 0\rangle \approx 0.87|22000\rangle + 0.32|20200\rangle + 0.30|20020\rangle.$$

Their energies with respect to the ground state of the neutral molecule (CAS(5,5) for the Hubbard hamiltonian) are respectively: -80 meV and -78 meV.

#### D. Electronic structure of product 2: CASCI calculations

The triplet and singlet many-body wavefunctions extracted from a CAS(6,6) are (here we only show occupancies of the orbitals 3 (HOMO) and 4(LUMO) because they are the most important ones within 96% accuracy for the triplet ground state and the first excited singlet state):

**Neutral molecule:**

$$|M_0, S_z = 0\rangle \approx 0.7|\uparrow\downarrow\rangle + 0.7|\downarrow\uparrow\rangle.$$

In the subspace  $S_z = 1$  it is simply to 96% of the Slater determinant:

$$|M_0, S_z = 1\rangle \approx |\uparrow\uparrow\rangle.$$

The excited singlet  $|M_1\rangle$ , on the other hand, is simply:

$$|M_1\rangle \approx 0.7|20\rangle + 0.7|02\rangle$$

(here the occupation numbers always refer to the orbitals 3(HOMO) and 4(LUMO)).

**Molecule with one extra electrons:** The two main multiplets in the subspace are

$$|M_0^+, S_z = 1/2\rangle \approx 0.78|2 \uparrow\rangle + 0.52|\uparrow 2\rangle,$$

$$|M_1^+, S_z = 1/2\rangle \approx -0.54|2 \uparrow\rangle + 0.81|\uparrow 2\rangle.$$

The energies of these multiplets with respect to the neutral Ground State are: 2.37eV and 2.41 eV

**Molecule with one less electron:** The two main multiplets are

$$|M_0^-, S_z = 1/2\rangle \approx 0.78|0 \uparrow\rangle + 0.52| \uparrow 0\rangle,$$

$$|M_1^-, S_z = 1/2\rangle \approx -0.54|0 \uparrow\rangle + 0.81| \uparrow 0\rangle.$$

The energies of these multiplets with respect to the neutral Ground State are: -1.91eV and -1.89eV.

### S3. IONIC ANDERSON HAMILTONIAN IN THE CHANNEL-ENERGY REPRESENTATION

In the discrete momentum space, the hybridization and conduction terms of the ionic Anderson Hamiltonian are

$$\hat{H}_{\text{con}} = \sum_{\mathbf{k}, \sigma} \epsilon_{\mathbf{k}} \hat{c}_{\mathbf{k}\sigma}^\dagger \hat{c}_{\mathbf{k}\sigma}, \quad (1)$$

$$\hat{H}_{\text{hyb}} = \sum_{M_i m_i} \sum_{M_f m_f} \sum_{\alpha, \mathbf{k}, \sigma} V_{\alpha \mathbf{k}} \langle M_f m_f | f_{\alpha\sigma}^\dagger | M_i m_i \rangle | M_f m_f \rangle \langle M_i m_i | c_{\mathbf{k}\sigma} + \text{h.c.}, \quad (2)$$

where  $\epsilon_{\mathbf{k}}$  is the energy of the conduction electrons,  $\hat{c}_{\mathbf{k}\sigma}$  ( $\hat{c}_{\mathbf{k}\sigma}^\dagger$ ) annihilates (creates) a conduction electron with momentum  $\mathbf{k}$  and spin  $\sigma$ , and  $V_{\alpha \mathbf{k}}$  is the amplitude of an electron tunneling from the MO  $\alpha$  to a conduction state with momentum  $\mathbf{k}$ . We begin by re-writing the sums in the continuous momentum space,

$$\sum_{\mathbf{k}} \epsilon_{\mathbf{k}} \hat{c}_{\mathbf{k}\sigma}^\dagger \hat{c}_{\mathbf{k}\sigma} \rightarrow \int d^3 k \epsilon_{\mathbf{k}} \hat{a}_{\mathbf{k}\sigma}^\dagger \hat{a}_{\mathbf{k}\sigma}, \quad (3)$$

$$\sum_{\mathbf{k}} V_{\alpha \mathbf{k}} \hat{a}_{\mathbf{k}\sigma} \rightarrow \nu^{\frac{1}{2}} \int d^3 k V_{\alpha \mathbf{k}} \hat{a}_{\mathbf{k}\sigma}. \quad (4)$$

where  $a_{\mathbf{k}\sigma}^{(\dagger)}$  is the annihilation (creation) operator in the continuous  $\mathbf{k}$ -space, normalized as  $\{a_{\mathbf{k}\sigma}^\dagger, a_{\mathbf{k}'\sigma}\} = \delta(\mathbf{k} - \mathbf{k}')$ , and  $\nu$  is the density of  $\mathbf{k}$  points. In order to change to the energy representation, we define the operators  $\hat{c}_{\epsilon \hat{\mathbf{k}}\sigma}^{(\dagger)} = |\nabla_{\mathbf{k}} \epsilon_{\mathbf{k}}|^{-\frac{1}{2}} a_{\mathbf{k}\sigma}^{(\dagger)}$ , where  $\hat{\mathbf{k}} = \mathbf{k}/|\mathbf{k}|$  and the right hand side is evaluated at  $\epsilon_{\mathbf{k}} = \epsilon$ . This allows us to write the equations above as

$$\int d^3 k \epsilon_{\mathbf{k}} \hat{a}_{\mathbf{k}\sigma}^\dagger \hat{a}_{\mathbf{k}\sigma} = \int d\epsilon \int ds_{\mathbf{k}} \epsilon \hat{c}_{\epsilon \hat{\mathbf{k}}\sigma}^\dagger \hat{c}_{\epsilon \hat{\mathbf{k}}\sigma} \quad (5)$$

$$\nu^{\frac{1}{2}} \int d^3 k V_{\alpha \mathbf{k}} \hat{a}_{\mathbf{k}\sigma} = \int d\epsilon \int \frac{ds_{\mathbf{k}}}{\sqrt{v(\mathbf{k})}} V_{\alpha \mathbf{k}} \hat{c}_{\epsilon \hat{\mathbf{k}}\sigma}, \quad (6)$$

where  $\int_{\epsilon} ds_{\mathbf{k}}$  represents an integral over the momentum space surface of  $\mathbf{k}$  points for which  $\epsilon_{\mathbf{k}} = \epsilon$ , and  $v^{-1}(\mathbf{k}) := v(\epsilon, \hat{\mathbf{k}}) = \nu |\nabla_{\mathbf{k}} \epsilon|_{\epsilon=\epsilon_{\mathbf{k}}}^{-1}$ . Based on Eq. 6, we define the channel-energy representation operators as

$$\hat{c}_{\epsilon\alpha\sigma} = \frac{1}{[\rho(\epsilon)]^{\frac{1}{2}} V_{\alpha}(\epsilon)} \int_{\epsilon} \frac{ds_{\mathbf{k}}}{\sqrt{v(\mathbf{k})}} V_{\alpha\mathbf{k}} \hat{c}_{\epsilon\hat{\mathbf{k}}\sigma}, \quad (7)$$

where

$$V_{\alpha}(\epsilon) = \left[ \frac{\int_{\epsilon} \frac{ds_{\mathbf{k}}}{v(\mathbf{k})} |V_{\alpha\mathbf{k}}|^2}{\int ds_{\mathbf{k}}} \right]^{\frac{1}{2}} \quad (8)$$

is the average of  $|V_{\alpha\mathbf{k}}|^2$  over the  $\epsilon_{\mathbf{k}} = \epsilon$  surface and

$$\rho(\epsilon) = \frac{\int_{\epsilon} \frac{ds_{\mathbf{k}}}{v(\mathbf{k})}}{\int_{\epsilon} ds_{\mathbf{k}}} \quad (9)$$

is the density of states per unit of energy. In general, these operators do not provide an orthonormal basis, since

$$\{\hat{c}_{\epsilon\alpha\sigma}^{\dagger}, \hat{c}_{\epsilon'\alpha'\sigma'}\} = \frac{\delta(\epsilon - \epsilon') \delta_{\sigma\sigma'}}{\rho(\epsilon) V_{\alpha}(\epsilon) V_{\alpha'}(\epsilon)} \int_{\epsilon_{\mathbf{k}}=\epsilon} \frac{ds_{\mathbf{k}}}{v(\mathbf{k})} V_{\alpha\mathbf{k}}^* V_{\alpha'\mathbf{k}}. \quad (10)$$

Nonetheless, we know from experimental measurements that the hybridization between the MOs  $\alpha$  is small, so we assume that

$$\int_{\epsilon} \frac{ds_{\mathbf{k}}}{v(\mathbf{k})} V_{\alpha\mathbf{k}} V_{\alpha'\mathbf{k}} \approx \rho(\epsilon) V_{\alpha}(\epsilon)^2 \delta_{\alpha\alpha'}, \quad (11)$$

which leaves us with an orthonormal basis that fulfils

$$\{c_{\epsilon\alpha\sigma}^{\dagger}, c_{\epsilon'\alpha'\sigma'}\} = \delta(\epsilon - \epsilon') \delta_{\alpha\alpha'} \delta_{\sigma\sigma'}. \quad (12)$$

Thus, in the channel-energy representation the full ionic Anderson Hamiltonian is

$$\begin{aligned} \hat{\mathcal{H}} &= \hat{H}_{\text{mol}} + \hat{H}_{\text{con}} + \hat{H}_{\text{hyb}}, \\ \hat{H}_{\text{mol}} &= \sum_M \sum_m \epsilon_M |Mm\rangle \langle Mm|, \\ H_{\text{con}} &= \sum_{\alpha\sigma} \int \epsilon \hat{c}_{\epsilon\alpha\sigma}^{\dagger} \hat{c}_{\epsilon\alpha\sigma} d\epsilon \\ H_{\text{hyb}} &= \sum_{M_i m_f} \sum_{M_f m_i} \sum_{\alpha\sigma} \int d\epsilon [\rho(\epsilon)]^{\frac{1}{2}} V_{\alpha}(\epsilon) \langle M_f m_f | f_{\alpha\sigma}^{\dagger} | M_i m_i \rangle | M_f m_f \rangle \langle M_i m_i | c_{\epsilon\alpha\sigma} + \text{h.c.}, \end{aligned} \quad (13)$$

where we have introduced the  $\hat{H}_{\text{mol}}$  containing the energies  $\epsilon_M$  of each molecular multiplet  $|Mm\rangle$ . The Hamiltonian used in the main paper is obtained from considering the hybridization and the density of states as constants by performing the changes  $V_{\alpha}(\epsilon) \rightarrow V$  and  $\rho(\epsilon) \rightarrow \rho$ .

## S4. EFFECTIVE KONDO COUPLING

### A. Schrieffer-Wolff transformation

The effective Kondo interaction for the ionic Anderson Hamiltonian to second order in perturbation theory takes the form

$$\hat{H}_K = \sum_{m_0, m'_0} \int_{-D}^D d\epsilon \int_{-D}^D d\epsilon' T(m_0, \epsilon\alpha i \leftarrow m'_0, \epsilon'\alpha' i') |M_0, m_0\rangle \langle M_0, m'_0| c_{\epsilon\alpha i}^\dagger c_{\epsilon'\alpha' i'} \quad (14)$$

where  $T(m_0, \epsilon\alpha i \leftarrow m'_0, \epsilon'\alpha' i')$  is the second order scattering amplitude corresponding to virtual processes where an incoming electron with quantum numbers  $\epsilon'$  (energy),  $\alpha'$  (channel) and  $i'$  (spin) is scattered off the molecule into a state with quantum numbers  $\epsilon$ ,  $\alpha$  and  $\sigma$ , and the molecule spin changes its spin from  $m'_0$  to  $m_0$ . This amplitude can be written as a sum of contributions from the intermediate excited multiplets,

$$T(m_0, \epsilon\alpha i \leftarrow m'_0, \epsilon'\alpha' i') = \sum_{M_c} T_{S_c}^{N_c}(m_0, \epsilon\alpha i \leftarrow m'_0, \epsilon'\alpha' i') \quad (15)$$

where  $T_{S_c}^{N_c}(m_0, \epsilon\alpha i \leftarrow m'_0, \epsilon'\alpha' i')$  is the amplitude for processes where the intermediate molecular state belongs to the  $M_c$  multiplet, which has occupation and spin quantum numbers  $N_c, S_c$ . The Feynman diagrams for such processes are given schematically in Fig. S10.

The general expressions for scattering through an intermediate state with one more electron ( $N_c = N_0 + 1$ ) and one less electron ( $N_c = N_0 - 1$ ) are

$$\begin{aligned} T_{S_c}^{N_0+1}(m_0, \epsilon\alpha i \leftarrow m'_0, \epsilon'\alpha' i') &= -\rho V^2 \frac{\langle M_0 | f_\alpha | M_c \rangle \langle M_c | f_{\alpha'}^\dagger | M_0 \rangle}{\epsilon_{M_c} - \epsilon_{M_0}} \\ &\times (\tfrac{1}{2}, i; S_0, m_0 + i' - i | S_c, m_0 + i') (\tfrac{1}{2}, i'; S_0, m_0 | S_c, m_0 + i'), \end{aligned} \quad (16)$$

$$\begin{aligned} T_{S_c}^{N_0-1}(m_0, \epsilon\alpha i \leftarrow m'_0, \epsilon'\alpha' i') &= \rho V^2 \frac{\langle M_0 | f_\alpha^\dagger | M_c \rangle \langle M_c | f_{\alpha'} | M_0 \rangle}{\epsilon_{M_c} - \epsilon_{M_0}} \\ &\times (\tfrac{1}{2}, i; S_c, m_0 - i' | S_0, m_0 - i' + i) (\tfrac{1}{2}, i'; S_c, m_0 - i' | S_0, m_0), \end{aligned} \quad (17)$$

where we have used the Wigner-Eckart theorem to decompose the excitation matrix elements as

$$\langle M_1, m_1 | f_{\alpha i}^\dagger | M_2, m_2 \rangle = \langle M_1 | f_\alpha^\dagger | M_2 \rangle (\tfrac{1}{2}, i; S_2, m_2 | S_1, m_1)^*, \quad (18)$$

where  $\langle M_1 | f_\alpha^\dagger | M_2 \rangle$  is the reduced matrix element with respect to spin symmetry. The

Clebsch-Gordan coefficients needed to evaluate the terms in Eqs. 16 and 17 are

$$\left(\frac{1}{2}, \pm\frac{1}{2}; S, M | S + \frac{1}{2}, M \pm \frac{1}{2}\right) = \sqrt{\frac{1}{2} \left(1 \pm \frac{M \pm \frac{1}{2}}{S + \frac{1}{2}}\right)} \quad (19)$$

$$\left(\frac{1}{2}, \pm\frac{1}{2}; S, M | S - \frac{1}{2}, M \pm \frac{1}{2}\right) = \mp \sqrt{\frac{1}{2} \left(1 \mp \frac{M \pm \frac{1}{2}}{S + \frac{1}{2}}\right)}. \quad (20)$$

We begin by evaluating  $T_{S_0 - \frac{1}{2}}^{N_0+1}(m_0, \epsilon\alpha i \leftarrow m'_0, \epsilon\alpha' i')$ , which yields

$$\begin{aligned} T_{S_0 - \frac{1}{2}}^{N_0+1}(m_0, \epsilon\alpha i \leftarrow m'_0, \epsilon\alpha' i') &= -\rho V^2 \frac{\langle M_0 | f_\alpha | M_c \rangle \langle M_c | f_{\alpha'}^\dagger | M_0 \rangle}{\epsilon_{M_c} - \epsilon_{M_0}} \\ &\times \begin{cases} -\frac{1}{S_0 + \frac{1}{2}} \frac{1}{2} m_0, & \text{if } i = i' = \frac{1}{2}, m_0 = m'_0, \\ +\frac{1}{S_0 + \frac{1}{2}} \frac{1}{2} m_0, & \text{if } i = i' = -\frac{1}{2}, m_0 = m'_0, \\ -\frac{1}{S_0 + \frac{1}{2}} \frac{1}{2} \sqrt{S_0(S_0 + 1) - m_0(m_0 - 1)}, & \text{if } i = \frac{1}{2}, i' = -\frac{1}{2}, m_0 = m'_0 - 1, \\ -\frac{1}{S_0 + \frac{1}{2}} \frac{1}{2} \sqrt{S_0(S_0 + 1) - m_0(m_0 + 1)}, & \text{if } i = -\frac{1}{2}, i' = \frac{1}{2}, m_0 = m'_0 + 1, \end{cases} \\ &= \rho V^2 \frac{\langle M_0 | f_\alpha | M_c \rangle \langle M_c | f_{\alpha'}^\dagger | M_0 \rangle}{(\epsilon_{M_c} - \epsilon_{M_0})(S_0 + \frac{1}{2})} \frac{1}{2} S_{m_0 m'_0}^a \sigma_{ii'}^a \end{aligned} \quad (21)$$

where we have ignored the contributions to the scattering potential. In order to obtain the final expression we have made use of the relations

$$\hat{S}^a \sigma_{ii'}^a = \frac{1}{2} (\hat{S}^+ \delta_{i, i+1} + \hat{S}^- \delta_{i, i-1}) + \hat{S}^z \sigma_{ii'}^z, \quad (22)$$

$$S_{m_0 m'_0}^+ = \sqrt{S_0(S_0 + 1) - m_0(m_0 + 1)} \delta_{m_0, m'_0+1} \quad (23)$$

$$S_{m'_0 m_0}^- = \sqrt{S_0(S_0 + 1) - m_0(m_0 - 1)} \delta_{m_0, m'_0-1} \quad (24)$$

$$S_{m_0 m'_0}^z = m_0 \delta_{m_0, m'_0}, \quad (25)$$

where  $\sigma$  are the Pauli matrices and the index  $a$  labels the components of the vectors, which are to be summed over when repeated. Following the same procedure for the remaining  $N_c, S_c$  combinations, we obtain

$$T_{S_0 - \frac{1}{2}}^{N_0-1}(m_0, \epsilon\alpha i \leftarrow m'_0, \epsilon\alpha' i) = \rho V^2 \frac{\langle M_0 | f_\alpha^\dagger | M_c \rangle^* \langle M_c | f_{\alpha'} | M_0 \rangle^*}{(\epsilon_{M_c} - \epsilon_{M_0}) S_0} \frac{1}{2} S_{m_0 m'_0}^a \sigma_{ii'}^a, \quad (26)$$

$$T_{S_0 + \frac{1}{2}}^{N_0+1}(m_0, \epsilon\alpha i \leftarrow m'_0, \epsilon\alpha' i) = -\rho V^2 \frac{\langle M_0 | f_\alpha | M_c \rangle \langle M_c | f_{\alpha'}^\dagger | M_0 \rangle}{(\epsilon_{M_c} - \epsilon_{M_0})(S_0 + \frac{1}{2})} \frac{1}{2} S_{m_0 m'_0}^a \sigma_{ii'}^a \quad (27)$$

$$T_{S_0 + \frac{1}{2}}^{N_0-1}(m_0, \epsilon\alpha i \leftarrow m'_0, \epsilon\alpha' i) = -\rho V^2 \frac{\langle M_0 | f_\alpha^\dagger | M_c \rangle^* \langle M_c | f_{\alpha'} | M_0 \rangle^*}{(\epsilon_{M_c} - \epsilon_{M_0})(S_0 + 1)} \frac{1}{2} S_{m_0 m'_0}^a \sigma_{ii'}^a \quad (28)$$

Substituting these scattering amplitudes into Eq. 14 and introducing the operator

$$\hat{\psi}_{\alpha i} = \int d\epsilon \rho^{\frac{1}{2}} \hat{c}_{\epsilon \alpha i}, \quad (29)$$

we can write the Kondo interaction as

$$\hat{H}_K = \frac{J_{\alpha\alpha'}}{2} \hat{S}^a \cdot \hat{\psi}_{\alpha i}^\dagger \sigma_{ii'}^a \hat{\psi}_{\alpha' i'}, \quad (30)$$

where

$$\hat{S}^a = \sum_{m_0, m'_0} S_{m_0, m'_0}^a |M_0 m_0\rangle \langle M_0 m'_0|, \quad (31)$$

$$J_{\alpha\alpha'} = \sum_{M_c} \frac{V^2}{\epsilon_{M_c} - \epsilon_{M_0}} C_{\alpha\alpha'}^{M_c} \quad (32)$$

$$C_{\alpha\alpha'}^{M_c} = \begin{cases} \frac{\langle M_0 || f_\alpha || M_c \rangle \langle M_c || f_\alpha^\dagger || M_0 \rangle}{(S_0 + \frac{1}{2})}, & \text{if } N_c = N_0 + 1, S_c = S_0 - \frac{1}{2}, \\ \frac{\langle M_0 || f_\alpha^\dagger || M_c \rangle^* \langle M_c || f_\alpha || M_0 \rangle^*}{S_0}, & \text{if } N_c = N_0 - 1, S_c = S_0 - \frac{1}{2}, \\ -\frac{\langle M_0 || f_\alpha || M_c \rangle \langle M_c || f_\alpha^\dagger || M_0 \rangle}{(S_0 + \frac{1}{2})}, & \text{if } N_c = N_0 + 1, S_c = S_0 + \frac{1}{2}, \\ -\frac{\langle M_0 || f_\alpha^\dagger || M_c \rangle^* \langle M_c || f_\alpha || M_0 \rangle^*}{(S_0 + 1)}, & \text{if } N_c = N_0 - 1, S_c = S_0 + \frac{1}{2}. \end{cases} \quad (33)$$

## B. Scaling equations for the coupling constants

In order to obtain the scaling equations for the coupling constants  $J_{\alpha\alpha'}$  and  $j_a$ , we apply the poor man's scaling method [7] to the Kondo interaction derived in the previous section. By integrating over second-order scattering processes where the intermediate electron lies in the energy range  $|\epsilon| \in [D - |\delta D|]$ , we obtain the differential scaling  $\delta H_K$  of the Kondo interaction,

$$\delta \hat{H}_K = \sum_{m_0, m'_0} \int_{-D}^D d\epsilon \int_{-D}^D d\epsilon' \delta T(m_0, \epsilon \alpha i \leftarrow m'_0, \epsilon' \alpha' i') |M_0, m_0\rangle \langle M_0, m'_0| \hat{c}_{\epsilon \alpha i}^\dagger \hat{c}_{\epsilon' \alpha' i'}, \quad (34)$$

where  $\delta T(m_0, \epsilon \alpha i \leftarrow m'_0, \epsilon' \alpha' i')$  is the sum over second order scattering amplitudes involving the creation of an intermediate particle ( $p$ ) with or hole ( $h$ ) with energy  $|\epsilon| \in [D - \delta D, D]$ :

$$\delta T(m_0, \epsilon \alpha i \leftarrow m'_0, \epsilon' \alpha' i') = \delta T^{(p)}(m_0, \epsilon \alpha i \leftarrow m'_0, \epsilon' \alpha' i') + \delta T^{(h)}(m_0, \epsilon \alpha i \leftarrow m'_0, \epsilon' \alpha' i'). \quad (35)$$

The Feynman diagrams associated to these scattering amplitudes are given in Fig. S11. Evaluating them, we obtain

$$\begin{aligned}
& m_0, \epsilon\alpha i \leftarrow m_0'', \epsilon''\alpha'', i'' \leftarrow m_0', \epsilon'\alpha' i' \\
\delta T^{(p)}(m_0, \epsilon\alpha i \leftarrow m_0', \epsilon'\alpha' i') &= \frac{1}{2}\rho J_{\alpha\alpha'} S_{m_0 m_0''}^a \sigma_{ii''}^a \frac{|\delta D|}{-D} \frac{1}{2}\rho J_{\alpha''\alpha'} S_{m_0'' m_0'}^a \sigma_{i''i'}^b \quad (36) \\
&= -\frac{1}{4}\rho^2 [J^2]_{\alpha\alpha'} (S^a S^b)_{m_0 m_0'} (\sigma^a \sigma^b)_{ii'} \frac{|\delta D|}{D}
\end{aligned}$$

for the scattering through intermediate states with an excited electron, where  $\rho|\delta D|$  is the number of particle states in the  $[D - |\delta D|, D]$  energy range. For the scattering through an intermediate state with the incoming electron plus an electron-hole pair, we have

$$\begin{aligned}
& m_0, \epsilon\alpha i \leftarrow m_0, \epsilon\alpha i, \epsilon''\alpha'' i'', \epsilon'\alpha' i' \leftarrow m_0', \epsilon'\alpha' i' \\
\delta T^{(h)}(m_0, \epsilon\alpha i \leftarrow m_0', \epsilon'\alpha' i') &= -\frac{1}{2}\rho J_{\alpha''\alpha'} S_{m_0 m_0''}^a \sigma_{i''i'}^a \frac{|\delta D|}{-D} \frac{1}{2}\rho J_{\alpha\alpha''} S_{m_0'' m_0'}^b \sigma_{ii''}^b \quad (37) \\
&= \frac{1}{4}\rho^2 [J^2]_{\alpha\alpha'} (S^a S^b)_{m_0 m_0'} (\sigma^b \sigma^a)_{ii'} \frac{|\delta D|}{D}.
\end{aligned}$$

Thus, the total amplitude is

$$\begin{aligned}
\delta T(m_0, \epsilon\alpha i \leftarrow m_0', \epsilon'\alpha' i') &= -\frac{1}{4}\rho^2 [J^2]_{\alpha\alpha'} (S^a S^b)_{m_0 m_0'} [\sigma^a, \sigma^b]_{ii'} \frac{|\delta D|}{D} \\
&= -\frac{1}{4}\rho^2 [J^2]_{\alpha\alpha'} (S^a S^b)_{m_0 m_0'} 2i\epsilon_{abc} \sigma_{ii'}^c \frac{|\delta D|}{D} \\
&= -\frac{1}{4}\rho^2 [J^2]_{\alpha\alpha'} i\epsilon_{abc} [S^a, S^b]_{m_0 m_0'} \sigma_{ii'}^c \frac{|\delta D|}{D} \\
&= -\frac{1}{4}\rho^2 [J^2]_{\alpha\alpha'} i\epsilon_{abc} i\epsilon_{abd} S_{m_0 m_0'}^d \sigma_{ii'}^c \frac{|\delta D|}{D} \\
&= \frac{1}{4}\rho^2 [J^2]_{\alpha\alpha'} 2\delta_{cd} S_{m_0 m_0'}^d \sigma_{ii'}^c \frac{|\delta D|}{D} \\
&= \frac{1}{2}\rho^2 [J^2]_{\alpha\alpha'} S_{m_0 m_0'}^c \sigma_{ii'}^c \frac{|\delta D|}{D}.
\end{aligned} \quad (38)$$

Introducing this in Eq. 34, we get

$$\begin{aligned}
\delta \hat{H}_K &= \sum_{m_0, m_0'} \int_{-D}^D d\epsilon \int_{-D}^D d\epsilon' \frac{1}{2}\rho^2 [J^2]_{\alpha\alpha'} \frac{|\delta D|}{D} S_{m_0 m_0'}^a \hat{c}_{\epsilon\alpha i}^\dagger \sigma_{ii'}^a \hat{c}_{\epsilon'\alpha' i'}. \\
&= \frac{1}{2}\rho [J^2]_{\alpha\alpha'} \frac{|\delta D|}{D} \hat{S}^c \hat{\psi}_{\alpha i}^\dagger \sigma_{ii'}^c \hat{\psi}_{\alpha' i'}.
\end{aligned} \quad (39)$$

By comparison with Eq. 34, we find

$$\delta J_{\alpha\alpha'} = \rho [J^2]_{\alpha\alpha'} \frac{|\delta D|}{D}. \quad (40)$$

In the diagonal channel basis, this reduces to the simple expression

$$\delta j_a = \rho j_a^2 \frac{|\delta D|}{D}, \quad (41)$$

Therefore, as the energy scale is lowered, the magnitude  $|j_a|$  of the coupling will grow in antiferromagnetically coupled channels ( $j_a > 0$ ) until reaching the characteristic perturbative divergence and slowly decrease in the ferromagnetically coupled channels ( $j_a < 0$ ).

### C. Analysis of the coupling for 1 and 2

In order to examine the effective coupling of **1** and **2** to the substrate in detail, we diagonalize the Kondo coupling. This allows us to represent the coupling in an eigenstate basis where the molecule behaves as a local moment coupled to several independent channels, meaning that conduction electrons in one such channel cannot be scattered to another channel. We call these new channels "eigenchannels" and we label them with the letter  $a$ , keeping  $\alpha$  for the channels that couple to each MO, which we call "MO channels". We shall determine (i) whether the coupling to the eigenchannels is AFM or FM, (ii) the relative strength of these eigenchannels, and (iii) the projection of these eigenchannels onto the MO channels.

We choose the possible energy values  $\epsilon_-$  and  $\epsilon_+$  by approximating them as  $\epsilon_- = \epsilon_-^0 - \mu$  and  $\epsilon_+ = \epsilon_+^0 + \mu$ , where  $\epsilon_-^0$  and  $\epsilon_+^0$  are the energies of the excited multiplets when the molecule is free, and  $\mu$  is the chemical potential introduced to model the coupling to the substrate. This leaves us with  $\mu$  as a parameter, which we allow to vary in the range where  $\epsilon_-, \epsilon_+ > 0$ , ensuring that the ground state does not change.

For **1**, using the data in Table I of the main paper, which corresponds to the channels  $\alpha = 2, 3, 4$  relevant for this molecule. we find that the coupling constant matrix is

$$\mathbf{J} = V^2 \begin{pmatrix} -\frac{0.40}{\epsilon_-} - \frac{0.29}{\epsilon_+} & -\frac{0.06}{\epsilon_+} & 0 \\ -\frac{0.06}{\epsilon_-} & \frac{1.13}{\epsilon_-} + \frac{0.51}{\epsilon_+} & 0 \\ 0 & 0 & -\frac{0.04}{\epsilon_-} - \frac{0.4}{\epsilon_+} \end{pmatrix} \quad (42)$$

We index the matrix elements  $\alpha = 2, 3, 4$  so that it matches the MO labeling. We immediately see that the  $\alpha = 4$  MO channel is an eigenchannel with a FM coupling to the molecule. We discard it, as it is irrelevant at low temperatures. In the upper block we find the eigenvalues  $j_2$  and  $j_3$ , which are shown Fig. S12. Using the free molecule energies  $\epsilon_-^0 = -80$  meV

and  $\epsilon_+^0 = 490$  meV, we find that the eigenvalue  $j_2$  is negative in the whole  $\mu$  window, so the coupling to the  $a = 2$  eigenchannel is FM;  $j_3$  is positive, so the coupling to  $a = 3$  is AFM. In Fig. S13 we show the mixing of the MO channels in the eigenchannels in terms of the quantities  $|U_{\alpha a}|^2$ , where  $U$  are the diagonalizing matrices that fulfil  $\mathbf{j} = U^\dagger \mathbf{J} U$ . As can be seen in the graphs, the eigenchannel 2 (3) couples almost exclusively to the MO channel 2 (3), hence the labeling of the eigenchannel. The coupling to the secondary channel is of the order of  $|U_{\alpha a}| \sim 10^{-3}$  for both eigenchannels.

For **2**, the coupling constant matrix calculated from the data on Table I of the main paper is given by

$$\mathbf{J} = V|{}^2 \begin{pmatrix} \frac{1.24}{\epsilon_-} + \frac{1.24}{\epsilon_+} & \frac{0.1}{\epsilon_-} + \frac{0.83}{\epsilon_+} \\ \frac{0.1}{\epsilon_-} + \frac{0.83}{\epsilon_+} & \frac{0.57}{\epsilon_-} + \frac{0.55}{\epsilon_+} \end{pmatrix}. \quad (43)$$

Using the free molecule energies  $\epsilon_-^0 = -45$  meV and  $\epsilon_+^0 = 500$  meV, we find the eigenvalues  $j_3$  and  $j_4$  shown in Fig. S14. Except for the near vicinity of the lower limit  $\mu = -500$  meV, which is well into the mixed valence regime, both eigenvalues are positive, which means both eigenchannels develop an AFM coupling with the molecular spin. The mixing of the MO channels in the eigenchannels is shown in Fig. S15. The mixing is larger for **2** than for **1** as a result of the relatively larger off-diagonal entries of  $\mathbf{J}$ , but it is still possible to identify a primary MO channel for each eigenchannel in the whole  $\mu$  region: the eigenchannel 3 (4) has its largest component in the MO channel 3 (4).

#### D. Relationship between the NTOs and the eigenchannels

Using the orbital indices  $\alpha$ , we can write the transition matrix elements from which we compute the NTOs as

$$\begin{aligned} T_{\alpha\alpha'}^{m_0} &= \langle M_0, m_0 - 1 | \hat{f}_{\alpha\downarrow}^\dagger \hat{f}_{\alpha'\uparrow} | M_0 m_0 \rangle. \\ &= \langle M_0 | |f_\alpha^\dagger f_{\alpha'}| | M_0 \rangle (1, -1; S_0, m_0 | S_0, m_0 - 1), \end{aligned} \quad (44)$$

where we have applied the Wigner-Eckart theorem to decompose the transition matrix element into a reduced part and a Clebsch-Gordan coefficient, taking into account that  $f_{\alpha\downarrow}^\dagger f_{\alpha'\uparrow}$  is a tensor operator with total spin (irrep) 1 and spin projection (partner number)  $-1$ . Since the transition matrix elements in complete and reduced form for a given  $m_0$  differ only in a constant Clebsch-Gordan factor, they have the same eigenvectors and therefore they give us the same NTOs.

We can also expand the transition matrix elements by introducing the identity operator  $\mathbf{I} = \sum_{M,m} |M, m\rangle \langle M, m|$ , which results in

$$\begin{aligned}
T_{\alpha\alpha'}^{m_0} &= \sum_{M,m} \langle M_0, m_0 - 1 | \hat{f}_{\alpha\downarrow}^\dagger | Mm \rangle \langle Mm | \hat{f}_{\alpha'\uparrow} | M_0 m_0 \rangle \\
&= \sum_{M_c} \langle M_0, m_0 - 1 | \hat{f}_{\alpha\downarrow}^\dagger | M_c, m_0 - \frac{1}{2} \rangle \langle M_c, m_0 - \frac{1}{2} | \hat{f}_{\alpha'\uparrow} | M_0 m_0 \rangle \\
&= \sum_{M_c} \langle M_0 | | \hat{f}_{\alpha}^\dagger | | M_c \rangle \langle M_c | | \hat{f}_{\alpha'} | | M_0 \rangle (\frac{1}{2}, +\frac{1}{2}; S_c, m_0 - \frac{1}{2} | S_0, m_0) (\frac{1}{2}, -\frac{1}{2}; S_c, m_0 - \frac{1}{2} | S_0, m_0 - 1) \\
&= S_{m_0-1, m_0}^- \sum_{M_c} \frac{\langle M_0 | | \hat{f}_{\alpha}^\dagger | | M_c \rangle \langle M_c | | \hat{f}_{\alpha'} | | M_0 \rangle}{2F(N_0 - 1, S_c, S_0)} \\
&= \langle S_0 | | S^- | | S_0 \rangle (1, -1; S_0, m_0 | S_0, m_0 - 1) \sum_{M_c} \frac{\langle M_0 | | \hat{f}_{\alpha}^\dagger | | M_c \rangle \langle M_c | | \hat{f}_{\alpha'} | | M_0 \rangle}{2F(N_0 - 1, S_c, S_0)},
\end{aligned} \tag{45}$$

where

$$F(N_c, S_c, S_0) = \begin{cases} (S_0 + \frac{1}{2}), & \text{if } N_c = N_0 + 1, S_c = S_0 - \frac{1}{2}, \\ S_0, & \text{if } N_c = N_0 - 1, S_c = S_0 - \frac{1}{2}, \\ -(S_0 + \frac{1}{2}), & \text{if } N_c = N_0 + 1, S_c = S_0 + \frac{1}{2}, \\ -(S_0 + 1), & \text{if } N_c = N_0 - 1, S_c = S_0 + \frac{1}{2} \end{cases} \tag{46}$$

contains the spin factor and the sign appearing in Eq. 33. The factors with  $N_c = N_0 + 1$  appear when we compute the matrix elements with the creation and annihilation operators commuted,

$$T_{\alpha\alpha'}^{m_0} = - \langle M_0, m_0 - 1 | f_{\alpha'\uparrow} f_{\alpha\downarrow}^\dagger | M_0 m_0 \rangle. \tag{47}$$

Putting together Eqs. 44 and 45, we arrive at the equivalent expressions

$$\langle M_0 | | f_{\alpha}^\dagger f_{\alpha'} | | M_0 \rangle = \langle S_0 | | S^- | | S_0 \rangle \sum_{M_c} \frac{\langle M_0 | | \hat{f}_{\alpha}^\dagger | | M_c \rangle \langle M_c | | \hat{f}_{\alpha'} | | M_0 \rangle}{2F(N_0 + 1, S_c, S_0)} \tag{48}$$

and

$$- \langle M_0 | | f_{\alpha} f_{\alpha'}^\dagger | | M_0 \rangle^* = \langle S_0 | | S^- | | S_0 \rangle \sum_{M_c} \frac{\langle M_0 | | \hat{f}_{\alpha} | | M_c \rangle^* \langle M_c | | \hat{f}_{\alpha'}^\dagger | | M_0 \rangle^*}{2F(N_0 - 1, S_c, S_0)} \tag{49}$$

for the reduced matrix elements computed by introducing intermediate excited multiplets with positive and negative charge, respectively. The reduced matrix element  $\langle S_0 | | S^- | | S_0 \rangle$  is constant, so we incorporate it in a new transition matrix  $\mathcal{T}$  that contains only multiplet

quantum numbers and gives us the same NTOs as the original transition matrix  $\mathbf{T}^{m_0}$ :

$$\begin{aligned}\mathcal{T}_{\alpha\alpha'} &:= \frac{2 \langle M_0 | f_\alpha^\dagger f_{\alpha'} | M_0 \rangle}{\langle S_0 | S^- | S_0 \rangle} = \sum_{M_c}^{N_c=N_0+1} \frac{\langle M_0 | \hat{f}_\alpha^\dagger | M_c \rangle \langle M_c | \hat{f}_{\alpha'} | M_0 \rangle}{F(N_0 + 1, S_c, S_0)} \\ &= -\frac{2 \langle M_0 | f_\alpha^\dagger f_{\alpha'} | M_0 \rangle^*}{\langle S_0 | S^- | S_0 \rangle} = \sum_{M_c}^{N_c=N_0-1} \frac{\langle M_0 | \hat{f}_\alpha | M_c \rangle^* \langle M_c | \hat{f}_{\alpha'}^\dagger | M_0 \rangle^*}{F(N_0 + 1, S_c, S_0)}.\end{aligned}\quad (50)$$

To establish a connection between the NTOs and the eigenchannels, we write the coupling constant matrix as

$$\mathcal{J}_{\alpha\alpha'} = V^{-2} J_{\alpha\alpha'} = \sum_{M_c}^{N_c=N_0-1} \frac{\langle M_0 | \hat{f}_\alpha^\dagger | M_c \rangle^* \langle M_c | \hat{f}_{\alpha'} | M_0 \rangle^*}{(\epsilon_{M_c} - \epsilon_{M_0}) F(N_0 - 1, S_c, S_0)} + \sum_{M_c}^{N_c=N_0+1} \frac{\langle M_0 | \hat{f}_\alpha | M_c \rangle \langle M_c | \hat{f}_{\alpha'}^\dagger | M_0 \rangle}{(\epsilon_{M_c} - \epsilon_{M_0}) F(N_0 + 1, S_c, S_0)}.\quad (51)$$

We observe two main differences between  $\mathcal{T}$  and  $\mathcal{J}$ : (i)  $\mathcal{J}$  contains energy factors  $(\epsilon_{M_c} - \epsilon_{M_0})^{-1}$  and (ii)  $\mathcal{T}$  can be equivalently obtained from projecting onto intermediate states with either  $N_c = N_0 - 1$  or  $N_c = N_0 + 1$ , while  $\mathcal{J}$  includes both types of terms. The similarity of the matrices is best observed in the case where all the multiplets with  $N_c = N_0 \pm 1$  particles are degenerate and have an energy  $E = (\epsilon_{M_c} - \epsilon_{M_0})$  which yields

$$\begin{aligned}\mathcal{J}_{\alpha\alpha'} &= \frac{1}{E} \left[ \sum_{M_c}^{N_c=N_0-1} \frac{\langle M_0 | \hat{f}_\alpha^\dagger | M_c \rangle^* \langle M_c | \hat{f}_{\alpha'} | M_0 \rangle^*}{F(N_0 - 1, S_c, S_0)} + \sum_{M_c}^{N_c=N_0+1} \frac{\langle M_0 | \hat{f}_\alpha | M_c \rangle \langle M_c | \hat{f}_{\alpha'}^\dagger | M_0 \rangle}{F(N_0 + 1, S_c, S_0)} \right] \\ &= \frac{1}{E} [\mathcal{T}_{\alpha\alpha'}^* + \mathcal{T}_{\alpha\alpha'}^*] \\ &= \frac{2}{E} \mathcal{T}_{\alpha\alpha'}^*.\end{aligned}\quad (52)$$

This shows that in the limit where all the excited multiplets are degenerate, both matrices contain equivalent information and therefore the same unitary transformation gives us the NTOs and the eigenchannels when applied to the orbital and conduction states, respectively. Furthermore, in Figs. S7 and S8 we show the numerical comparison between these orbitals and corresponding  $dI/dV$  maps. In the case of **1**, the agreement is good for the NTOs and the Kondo orbitals. The main difference in the  $dI/dV$  maps is the brighter contrast in the central part presented by the Kondo orbitals, which fits better to the experimental evidence (see Fig. 1 in the main text). In the case of **2**, we found no apparent difference between both  $dI/dV$  maps.

## S5. NRG CALCULATIONS

### A. Method

For the NRG calculations we use a discretized Anderson Hamiltonian with the conduction and hybridization terms given by

$$\begin{aligned}\hat{H}_{\text{con}} &= \sum_{n=1}^{\infty} \tau_{n,\alpha} \hat{c}_{n,\alpha\sigma}^\dagger \hat{c}_{n+1,\alpha\sigma} + \text{h.c.}, \\ \hat{H}_{\text{hyb}} &= \sum_{M_i, M_f} \sum_{m_i, m_f} \sqrt{2\Gamma/\pi} \langle M_f, m_f | \hat{f}_{\alpha\sigma}^\dagger | M_i, m_i \rangle | M_f, m_f \rangle \langle M_i, m_i | \hat{c}_{1,\alpha\sigma} + \text{h.c.},\end{aligned}\tag{53}$$

where  $\Gamma = \pi\rho V^2$  is the constant hybridization; repeated indices are to be summed over. The term  $\hat{H}_{\text{con}}$  represents the conduction channels as a semi-infinite tight-binding chains, which are obtained using the interleaved discretization procedure [8]. Electrons in the  $n$ -th site of this chain are annihilated (created) by the operators  $\hat{c}_{n,\alpha\sigma}^{(\dagger)}$ . Neighboring sites are coupled by the hopping constants  $\tau_{n,\alpha}$ . The hybridization term  $\hat{H}_{\text{hyb}}$  couples the molecule to the first site in the chain. For all the calculations we use a half-bandwidth of  $D = 1\text{eV}$ .

We use the PointGroupNRG code [9] to compute the zero-temperature spectral functions and the thermodynamic curves (given below) following the procedure presented in Ref. [10]. The spectral function, shown in Fig. 4 of the main paper, is defined as

$$A_\alpha(\epsilon) = \sum_\sigma \sum_E \left[ |\langle E | \hat{f}_{\alpha\sigma}^\dagger | G \rangle|^2 \delta(\epsilon - (\epsilon_E - \epsilon_G)) + |\langle E | \hat{f}_{\alpha\sigma} | G \rangle|^2 \delta(\omega + (\epsilon - \epsilon_G)) \right], \tag{54}$$

where  $|E\rangle$  is an excited state,  $|G\rangle$  is the ground state. The calculation is performed by choosing for each NRG iteration  $n$  a value  $\epsilon_n = 2\omega_n$  for which the spectral function is computed, where  $\omega_n$  is the energy scale corresponding to the  $n$ -th step. The delta peaks are broadened using a Gaussian kernel with

$$\delta(\epsilon) \rightarrow \frac{1}{\eta_n \sqrt{\pi}} \exp \left[ -(\epsilon/\eta_n)^2 \right], \tag{55}$$

where  $\eta_n = \omega_n$  is chosen as the broadening factor. The results are averaged over 4 values of the twisting parameter  $z$  in order to improve the smoothness of the curves. For the thermodynamic functions, smooth curves are obtained by averaging over even and odd NRG steps. For both spectral and thermodynamic calculations, we use a discretization parameter  $\Lambda = 3$  and a cutoff of 1000 multiplets.

## B. Thermodynamic curves and Kondo temperatures

To provide further insight into the Kondo effect, we show the thermodynamic curves for **1** and **2**. These have been computed using the same parameters  $\pi\rho|V|^2$  and  $\mu$  used in the calculation of the spectral functions.

The calculated entropy and magnetic susceptibility curves for **1** are shown in Fig. S16a. These curves show that the system develops a local moment around  $k_B T/D \sim 10^{-2}$ , in the region where the entropy and magnetic susceptibility are close to the local moment fixed point values  $S/k_B = \ln(2)$  and  $k_B T\chi/(g\mu_B)^2 = 1/4$ . At lower temperatures this local moment is screened, with the full screening corresponding to the values  $S = \chi = 0$ . The Kondo temperature  $T_K$  obtained from the magnetic susceptibility, calculated as the point where  $d\chi/dT|_{T=T_K} = 0$ , is  $T_K \approx 5K$ . This is close to the value  $T_K \approx 8K$  calculated from the full width at half-maximum  $\Delta$  of the peak in the MO 3 spectral function,  $k_B T_K = \Delta$ . Both values agree with the Kondo temperature obtained by fitting to the experimental results, which lies in the  $T_K \in [1, 10]K$  range.

Thermodynamic curves for **2** are shown in Fig. S16b. As the temperature is decreased, the magnetic susceptibility curve starts approaching the  $3/4$  value of the spin-1 local moment fixed point, which has an associated entropy  $S/k_B = \ln(3)$ . The hybridization rapidly causes this tendency to shift, screening the partially formed local moment. Two stages can be observed in the screening, separated by the middle inflexion point in the magnetic susceptibility curve, in agreement with the anisotropy in the  $j_a$  eigenvalues found in section S4C. This is a characteristic feature of the spin-1 local moment anisotropic Kondo effect[11].

It must be noted that, for both **1** and **2**, the large hybridization  $\Gamma \sim \epsilon_{\pm}$  causes the system to evolve to the screened regime without fully developing the local moment. If the hybridization were smaller, we would observe a plateau close to the local moment fixed point values for a large portion of the temperature range. In principle, this would mean that the effective model is not a good approximation. Nevertheless, the results for the spectral functions agree with the analysis based on the effective Kondo model with respect to the nature of the magnetic coupling to the channels 2 and 3 (FM or AFM). Thus, the rationalization

of the Kondo peaks based on the Kondo model can be considered as qualitatively correct.

---

- [1] A. Cahlik, Kondo fit, [https://github.com/cahlikales/Kondo\\_fit](https://github.com/cahlikales/Kondo_fit).
- [2] H. Frota, Physical Review B **45**, 1096 (1992).
- [3] M. Gruber, A. Weismann, and R. Berndt, Journal of Physics: Condensed Matter **30**, 424001 (2018).
- [4] J. Kondo, Progress of theoretical physics **32**, 37 (1964).
- [5] R. L. Martin, The Journal of Chemical Physics **118**, 4775 (2003).
- [6] O. Krejčí, P. Hapala, M. Ondráček, and P. Jelínek, Physical Review B **95**, 10.1103/physrevb.95.045407 (2017).
- [7] P. W. Anderson, J. Phys. C: Solid St. Phys **3** (1970).
- [8] M. Yoshida, M. A. Whitaker, and L. N. Oliveira, Phys. Rev. B **41**, 9403 (1990).
- [9] A. Calvo-Fernández, M. Blanco-Rey, and A. Eiguren, The PointGroupNRG code for numerical renormalization group calculations with discrete point-group symmetries (2023), arXiv:2307.03658 [cond-mat.str-el].
- [10] R. Bulla, T. A. Costi, and T. Pruschke, Rev. Mod. Phys. **80**, 395 (2008).
- [11] C. Jayaprakash, H. R. Krishna-murthy, and J. W. Wilkins, Phys. Rev. Lett. **47**, 737 (1981).

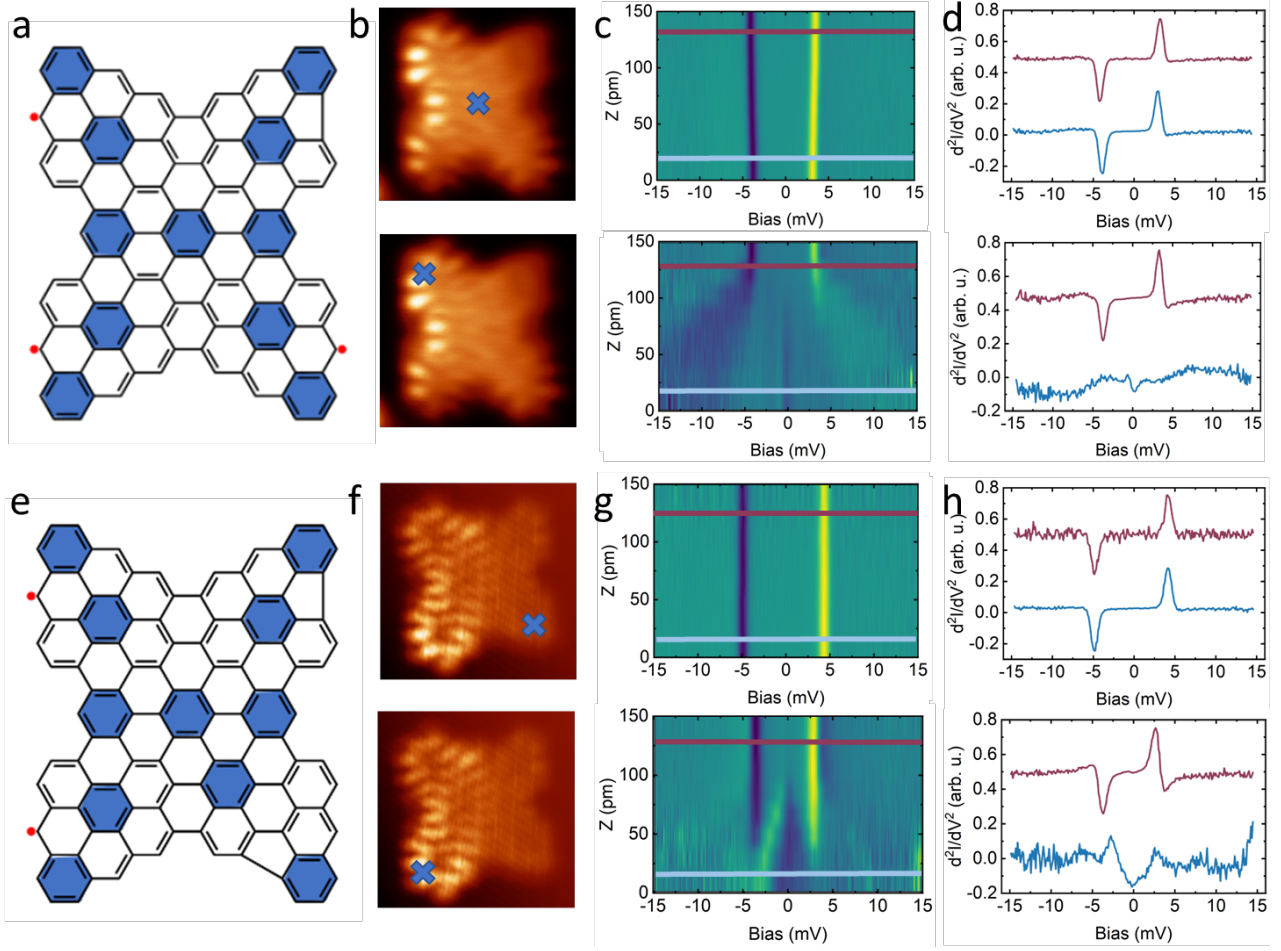


FIG. S1:  $d^2I/dV^2$  IETS spectra of **1** and **2** on Au(111) acquired with NiCp<sub>2</sub>-functionalized tip. (a, e) Chemical schemes of **1** and **2** molecules. Constant height STM images of **1** at 3.4 mV (b) and **2** at 1 mV (f), image size:  $2.5 \times 2.5$  nm<sup>2</sup>. (c, g) Experimental  $d^2I/dV^2(z)$  IETS taken with NiCp<sub>2</sub>-functionalized tip in the positions marked by blue crosses in top and bottom panels of (b, f) respectively. (d, h)  $d^2I/dV^2$  curves for selected heights in (c, g) marked with the horizontal lines. Red/blue colored lines in (c, g) correspond to red/blue spectra in (d, h). While the NiCp<sub>2</sub>  $d^2I/dV^2(z)$  IETS remains unaltered when approaching to a non magnetic site of the molecules (b top, f top), it deforms on the edge providing a fingerprint of the local magnetic signal originated from the Kondo effect[4] (b bottom, f bottom).

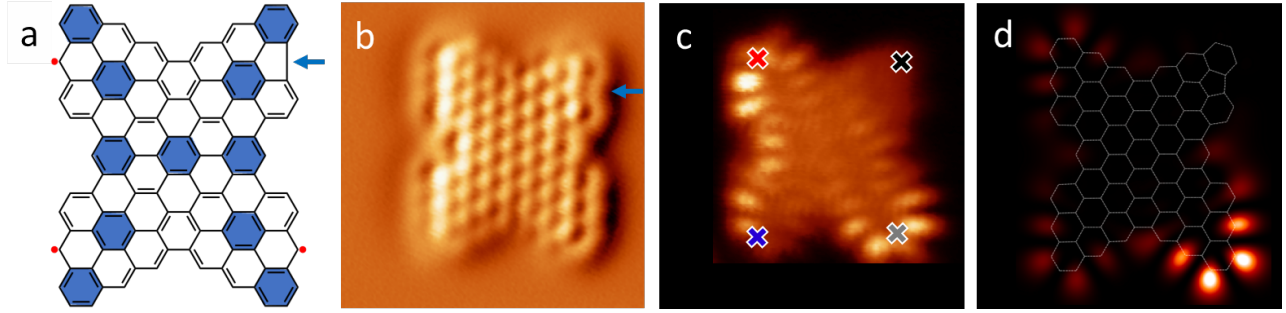


FIG. S2: **Spin-excitation signal from the doublet ground state to the first excited quartet state of molecule 1.** a) scheme of the molecule, blue lines highlight the location of the defect. Simultaneously recorded high resolution CO tip AFM (b) and  $dI/dV$  map (c) images of the molecule **1** acquired at 24 meV, size:  $3 \times 3 \text{ nm}^2$ . It should be noted that the signal on the left edge in the experimental  $dI/dV$  map is caused by the presence of the Kondo resonance located at the Fermi energy. Thus, the appearance of the signal on the left edge has nothing to do with spin excitation from the ground state to the first excited state. d) simulated spin excitation map obtained from the Natural Transition Orbitals for the spin flip operator between the ground state doublet and the first excited quartet state, see Figure S5.

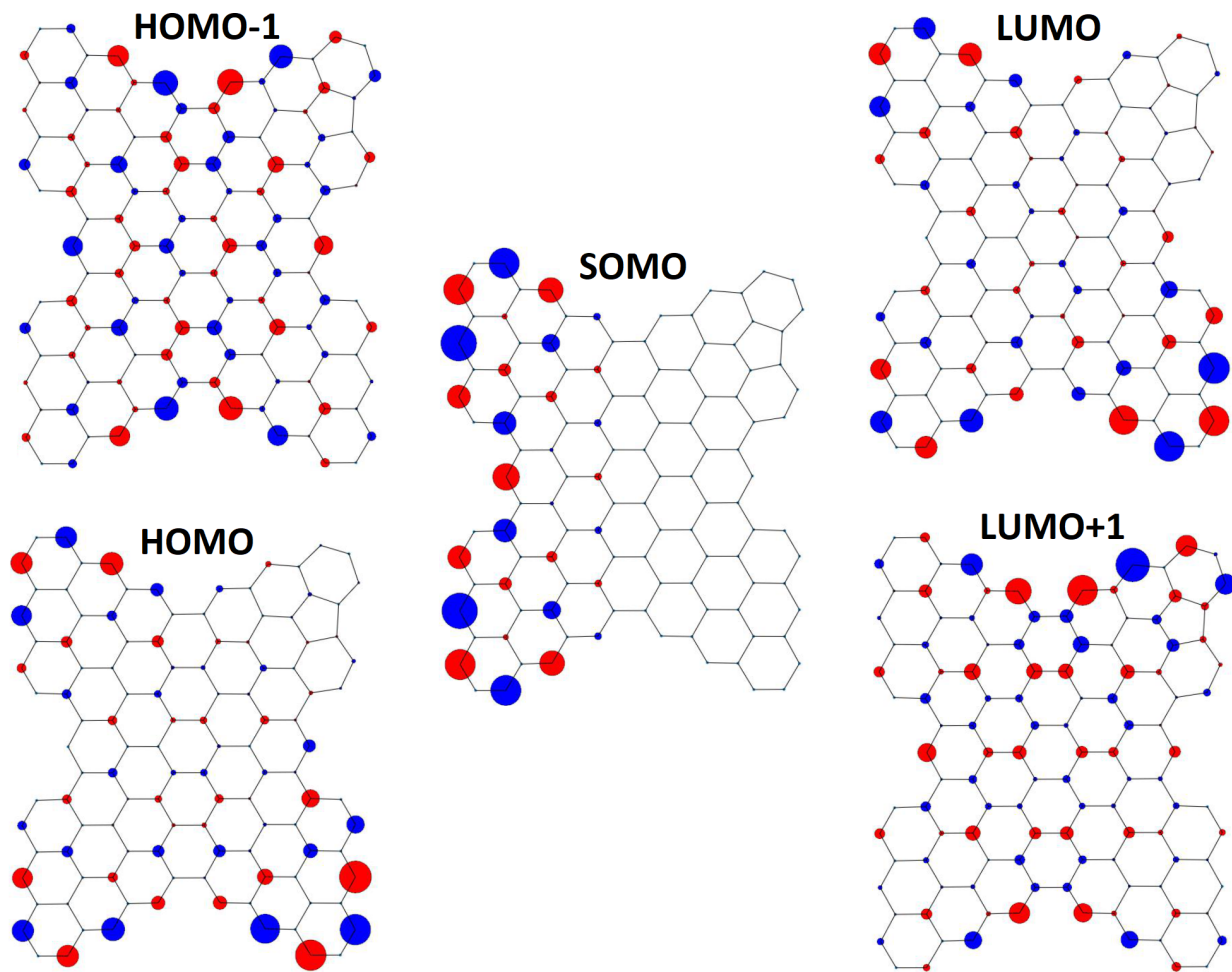


FIG. S3: Single electron Hückel orbitals used for the Hubbard-CAS calculations in product 1: 1 (HOMO-1), 2(HOMO), 3(SOMO), 4(LUMO), 5(LUMO+1). The numbering of orbitals is according to the Figure 2 in the main text.

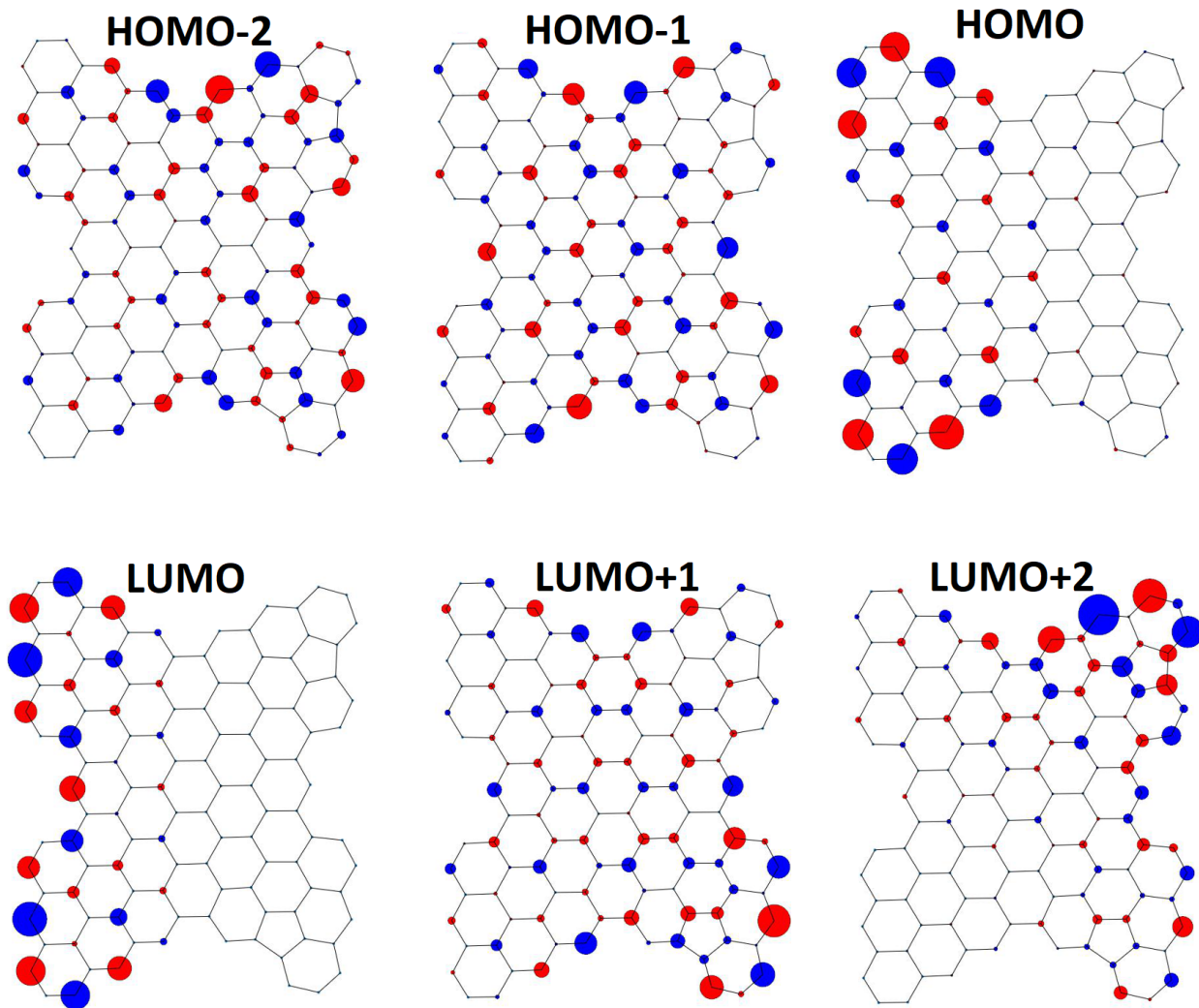


FIG. S4: **Single electron Hückel orbitals used for the Hubbard-CAS calculations in product 2.** First row, from left to right displays as follows : 1 (HOMO-2), 2(HOMO-1) and 3(HOMO). Second row, from left to right: 4 (LUMO), 5(LUMO+1), 6(LUMO+2).

The numbering of orbitals is according to the Figure 2 in the main text.

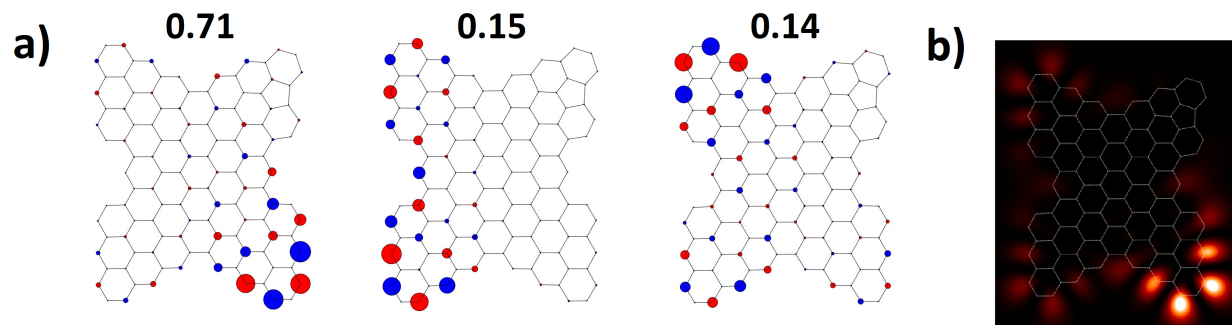


FIG. S5: **Calculated NTO and  $dI/dV$  maps of the doublet to quartet spin excitation of molecule 1** a) Three dominant (from left to right) NTO orbitals for the doublet-quartet spin excitation of product **1**, each with their corresponding weights, b) resulting simulated  $dI/dV$  map obtained from these NTOs.

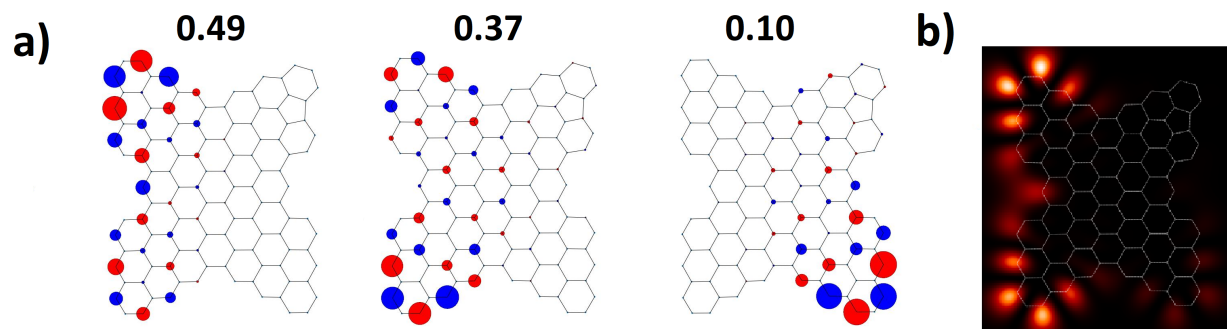


FIG. S6: **Calculated NTO and  $dI/dV$  maps of the doublet to doublet spin flip of molecule 1.** a) Three dominant (from left to right) NTO orbitals for the spin flip between two degenerate ground state doublets that yields the Kondo effect in product **1** with their respective weights, b) simulated  $dI/dV$  map obtained from these orbitals

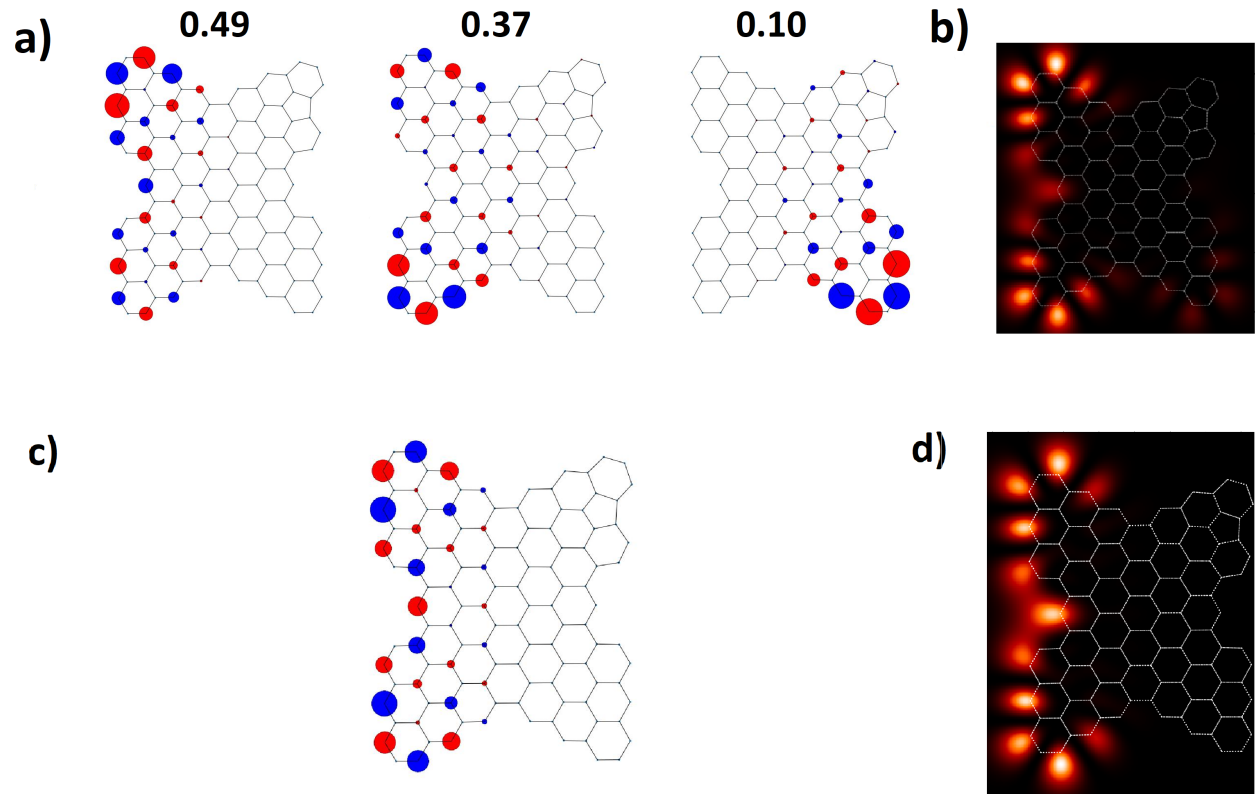


FIG. S7: Comparison of  $dI/dV$  maps obtained from NTO and the Kondo channel for molecule 1. a) NTO orbitals with their weight and b) corresponding simulated  $dI/dV$  map. c) the Kondo channel obtained from the diagonalization of the  $J$  matrix, and d) the corresponding simulated  $dI/dV$  map.

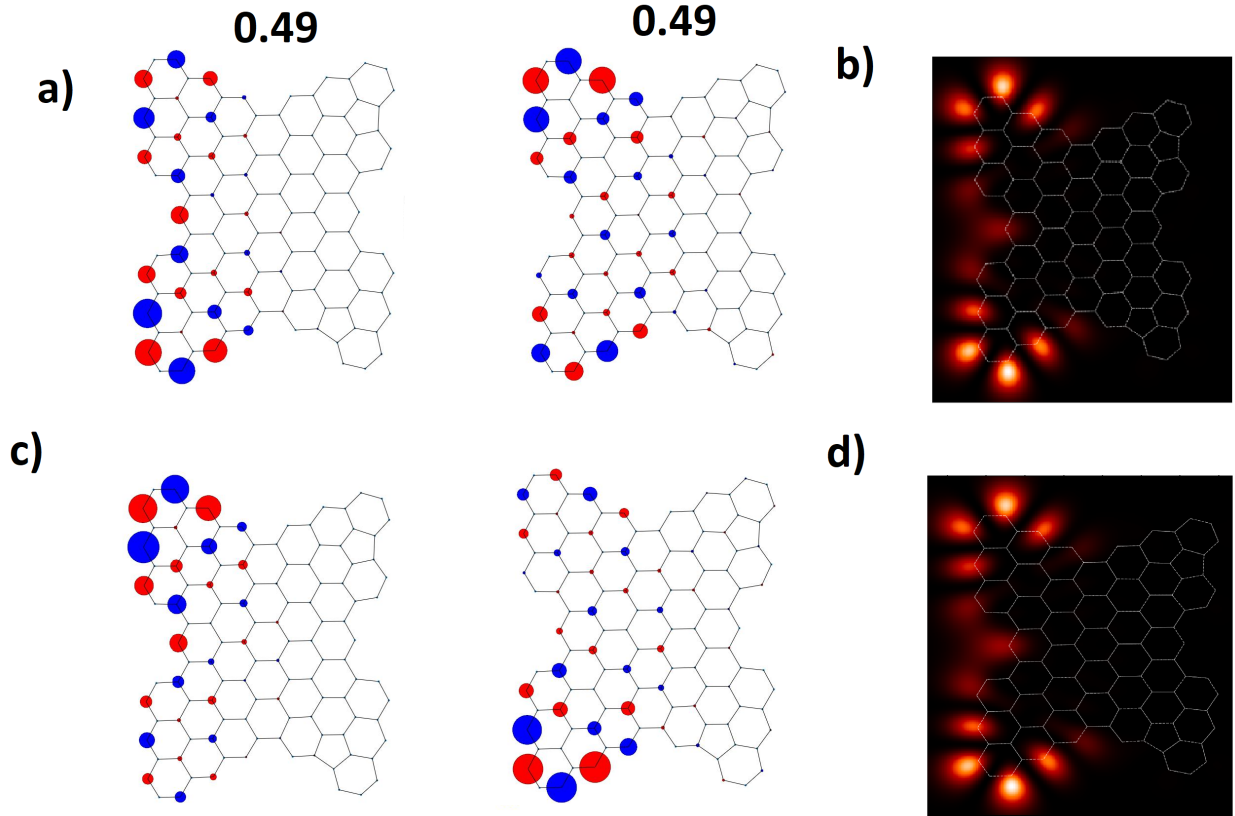


FIG. S8: Comparison of  $dI/dV$  maps obtained from NTO and two Kondo channels for molecule **2**. a) NTO orbitals with their weight and b) corresponding simulated  $dI/dV$  map, c) two Kondo channels obtained from the diagonalization of the  $J$  matrix and d) the corresponding simulated  $dI/dV$  map.

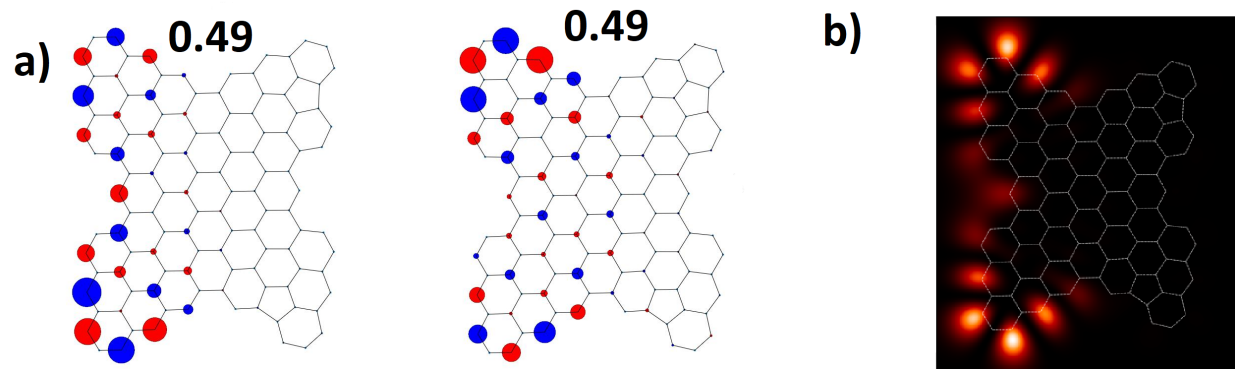


FIG. S9: Calculated NTO and  $dI/dV$  maps of the doublet to doublet spin flip of molecule **2**. a) Two dominant (from left to right) NTO orbitals for the spin flip between two degenerate ground state doublets that yields the Kondo effect in product **2** with their respective weights, b) simulated  $dI/dV$  map obtained from these two NTOs.

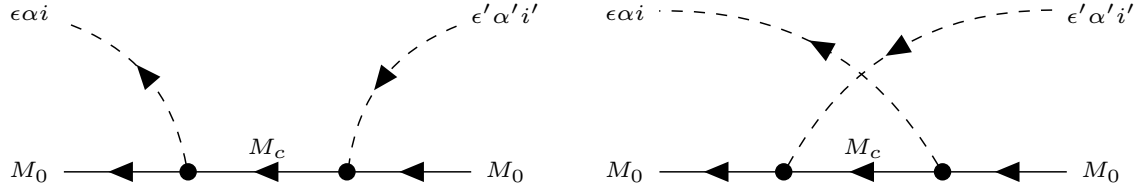


FIG. S10: Schematic Feynman diagrams for virtual scattering process through the intermediate molecular multiplet  $M_c$  with  $N_c = N_0 + 1$  (left) and  $N_c = N_0 - 1$  (right).

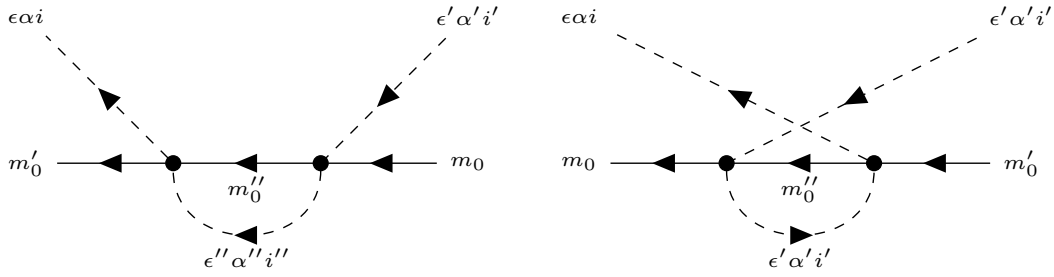


FIG. S11: Feynman diagrams for virtual processes with an intermediate electron (left) and hole (right).

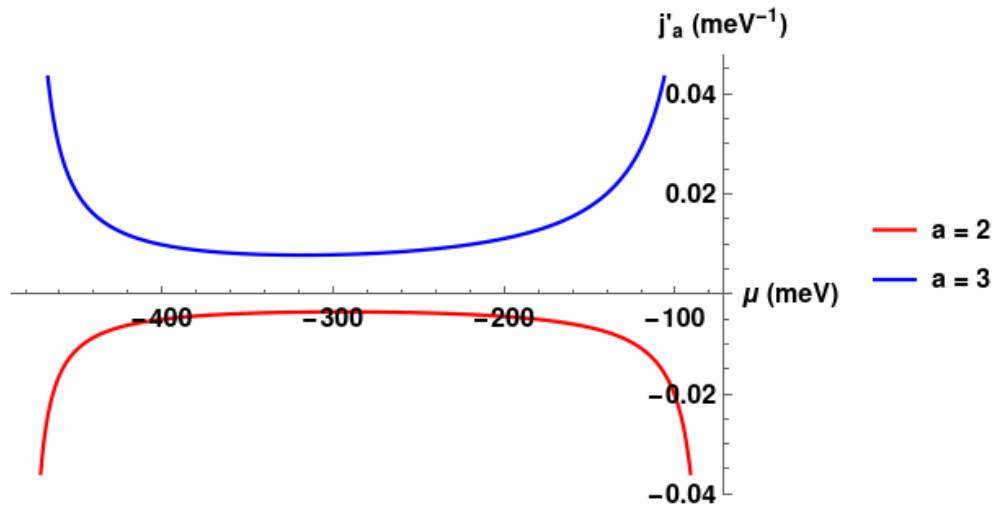


FIG. S12: Eigenvalues  $j'_2 = V^{-2}j_2$  and  $j'_3 = V^{-2}j_3$  for  $\mathbf{1}$ .

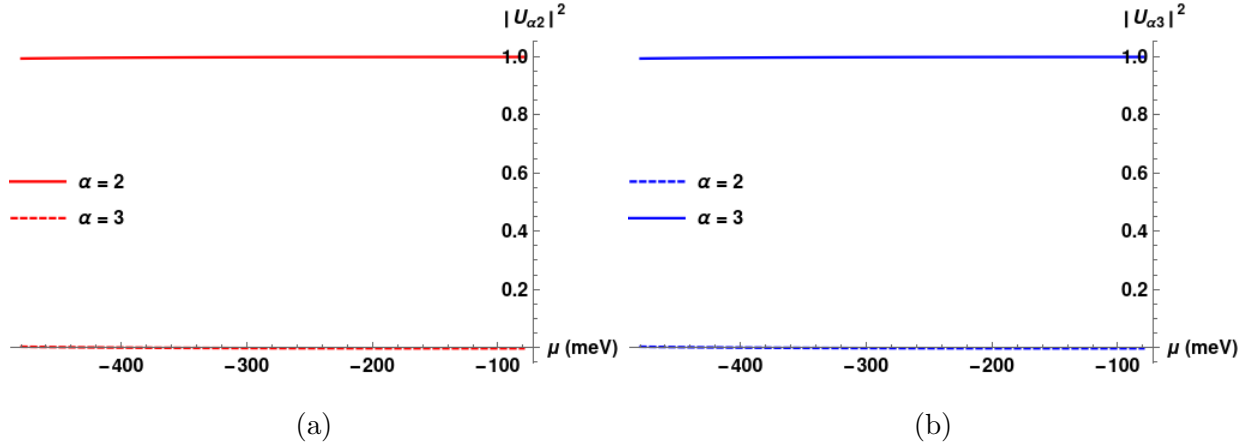


FIG. S13: For **1**, MO channel mixings  $|U_{\alpha a}|^2$  for the eigenchannels  $a = 2$  (a) and  $a = 3$  (b) and the primary (thick) and secondary (dashed) MO channels  $\alpha = 2, 3$ .

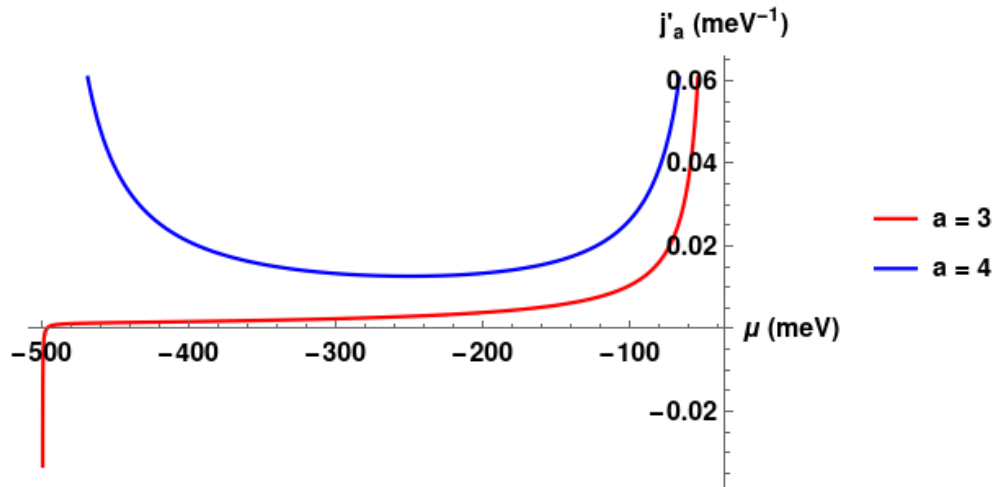


FIG. S14: Eigenvalues  $j'_3 = V^{-2}j_3$  and  $j'_4 = V^{-2}j_4$  for **2**.

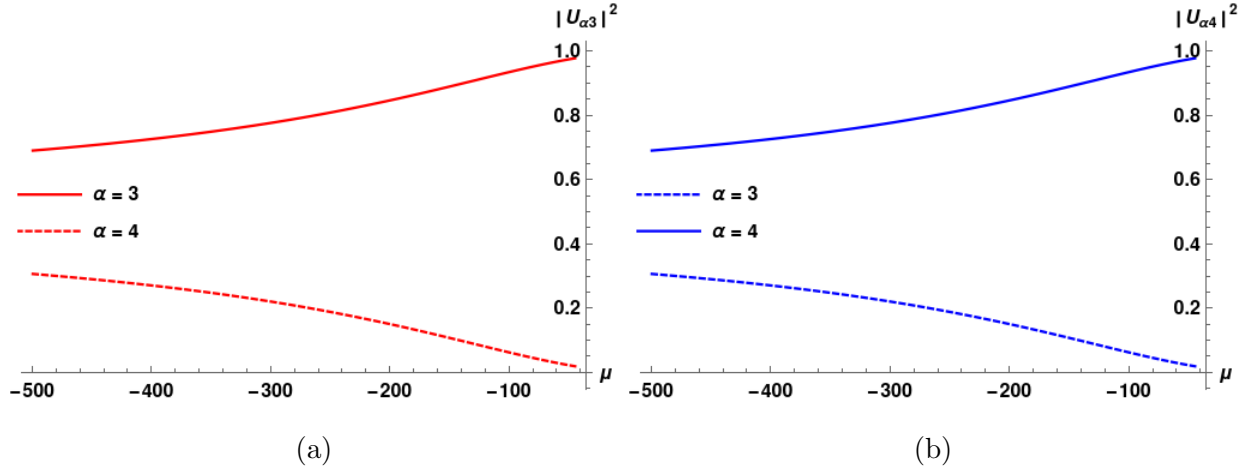
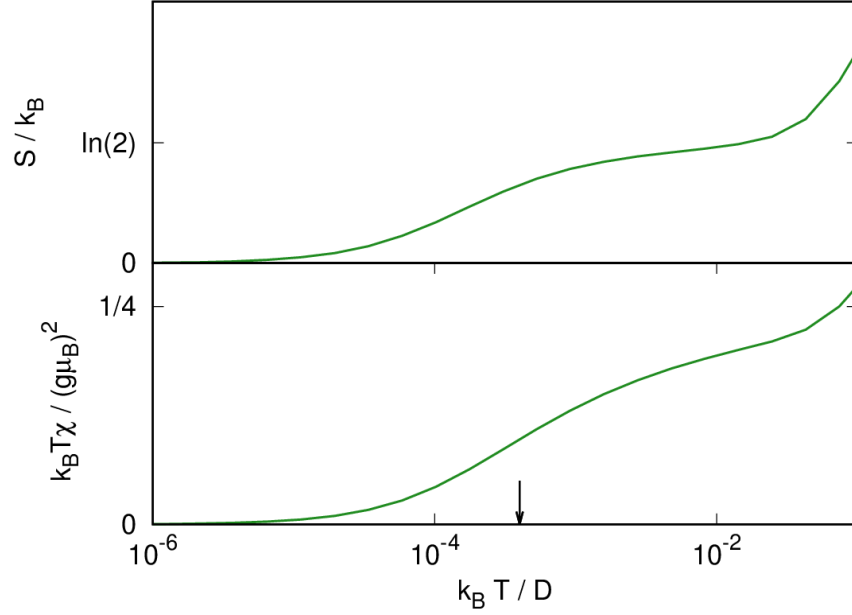
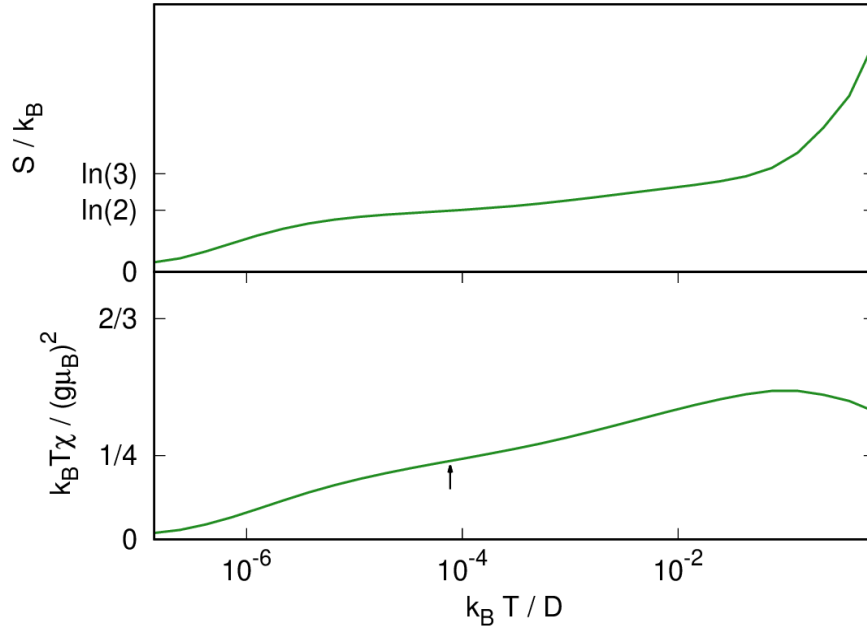


FIG. S15: For **2**, MO channel mixings  $|U_{\alpha a}|^2$  for the eigenchannels  $a = 3$  (a) and  $a = 4$  (b) and the primary (thick) and secondary (dashed) MO channels  $\alpha = 3, 4$ .



(a)



(b)

FIG. S16: Calculated thermodynamic functions for molecules **1** (a) and **2** (b): entropy (top panel) and magnetic susceptibility (bottom panel). The parameters are  $\Gamma = 0.1$  eV for **1**,  $\Gamma = 0.15$  eV for **2**, and  $\mu = -0.2$  eV for both. The arrow in (a) indicates the Kondo temperature  $k_B T_K = 4 \times 10^{-4}$  eV. The arrow in (b) indicates the separation between the two screening stages.